VISIBLE VERSUS NEAR-INFRARED LIGHT PENETRATION DEPTH ANALYSIS

IN AN INTRALIPID SUSPENSION AS IT RELATES

TO CLINICAL HYPERSPECTRAL IMAGES

by

TINSY JOHN PERUMANOOR

Presented to the Faculty of the Graduate School of

The University of Texas at Arlington

in Partial Fulfillment of the Requirements for the Degree of

MASTER OF SCIENCE IN BIOMEDICAL ENGINEERING

THE UNIVERSITY OF TEXAS AT ARLINGTON

AUGUST 2008

Lastly, but most importantly, I thank my parents and sisters for the care and support they have given in all endeavors of my life. To them, I dedicate this work.

July 14, 2008

ABSTRACT

VISIBLE VERSUS NEAR-INFRARED LIGHT PENETRATION DEPTH ANALYSIS

IN AN INTRALIPID SUSPENSION AS IT RELATES TO

CLINICAL HYPERSPECTRAL IMAGES

Tinsy John Perumanoor, M. S.

The University of Texas at Arlington, 2008

Supervising Professor: Dr. Karel J. Zuzak

We determine the penetration depth of near-infrared and visible light in a tissue phantom model using various image processing techniques and chemometrics and use these results to demonstrate the application of a multimodal hyperspectral imaging system for monitoring blood perfusion in amputation wounds. It is capable of performing a noninvasive, *in vivo*, quantitative analysis of human tissue in a clinical environment, in terms of the percent saturation of oxyhemoglobin. The instrument majorly consists of near-infrared and visible charge coupled devices (CCDs), lenses, liquid crystal tunable filters (LCTFs) for both the CCDs attached to their respective lenses, and a broad band light source. A 1% intralipid suspension, which mimics the skin-tissue interface and india ink, a good absorber of light are used to create the phantom model and experiments are done using this model to determine the penetration depth of near-infrared and visible

light, by collecting hyperspectral image cubes using the hyperspectral instrument and analyzing it. Different methods of analyses are done on the image data cubes collected and the results prove that the near-infrared light penetrates deeper into tissues than visible. This result is used to demonstrate the ability of the hyperspectral imager to clinically monitor human lower limb amputation wounds and determine the perfusion of oxygenated blood in it. In other words, it can monitor amputation wounds based on the level of oxyhemoglobin saturation in the tissues.

TABLE OF CONTENTS

LIST OF ILLUSTRATIONS

LIST OF TABLES

CHAPTER 1

INTRODUCTION

1.1 Amputation

Amputation is the traumatic or surgical removal of a body extremity. It is a commonly performed surgery especially on old people. There are several reasons for the surgical removal of a limb in the human body. In most cases, an amputation is done to control pain or a disease process in the affected limb, such as malignancy or gangrene [1]. Gangrene is a complicated form of cell death, characterized by the decay of body tissues, which become black and malodorous. The reasons for these conditions can be infection or ischemia, which, very often is associated with diabetes and long-term smoking. This condition is most common in the lower extremities. Amputation is also carried out in some individuals as a preventive measure for such conditions [2]. Figure 1 shows two different types on amputations performed on patients, in which A is performed above the knee and B shows amputated toes.

A   **B**

Figure 1. A shows amputation performed above the knee (above knee amputation, AKA), and B shows amputated toes

1.2 Wound healing

Estimating the tissue oxygenation or amount of oxygen saturation in blood is a good measure of predicting the healing of a wound. Hyperspectral imaging is one of the latest tools that can be used to non-invasively quantify healing in this manner [3, 4]. It has various uses in amputations, as will be explained in the respective sections.

1.3 Monitoring amputation wounds

This research majorly focuses on determining the penetration depth of near-infrared and visible light in tissue phantom models and using this information to monitor amputation wounds over a period of time in terms of oxyhemoglobin (HbO_2) saturation, or, in simple words, perfusion of blood having good amount of oxygen saturation. The technique used for this viz. hyperspectral imaging may also be put to use for determining the point on the limb at which amputation has to be done based on the level of percent HbO_2, prior to amputation. The imager used in this research is called "multimodal", by virtue of the two cameras used in it, one operating in the near-infrared light range and another, in the visible range.

This being the utility of the system, a major question arising out of it is, "how deep into the tissues can such an imager see"? The depth of penetration of near-infrared light and visible light cannot be directly measured in human tissues. Therefore, a phantom model which mimics the properties of a skin-tissue interface was prepared and experiments done with it to determine the penetration depth. This model would closely approximate the properties of the human tissue imaged in the real application explained above.

Intralipid[TM] 20%, an intravenous fat emulsion diluted down to a concentration of 1% using distilled water is used as a skin-tissue model [5, 6, 7] and blue india ink[TM] as an absorber of light [7, 8], which mimics blood vessels and capillaries in the tissue.

The intralipid phantom model is illuminated with a broad band light and the multimodal hyperspectral imaging system is employed to collect image cubes (explained in section 1.4) with the absorber at different depths in the intralipid suspension, to determine the penetration depth of near-infrared and visible light. Various techniques (methods of analyses) like computing the contrast-to-background ratio (CBR) and signal-to-noise ratio (SNR) have been deployed for finding out the penetration depth of both near-infrared and visible light in the intralipid tissue model.

Similar types of analyses is also done by keeping the capillary filled with ink at different depths under animal fat layers, to confirm the principle of near-infrared light penetrating deeper than visible. The results of these analyses (in the phantom model and fat) are then used to monitor real amputation wounds in terms of tissue oxygenation in both the deeper and superficial tissues.

1.4 Hyperspectral imaging

Hyperspectral imaging is an emerging technique in the field of medicine, which enables the integrated use of spatial and spectral methods. Hyperspectral imaging can be used to acquire images over a spectral band of multiple wavelengths, generating precise optical spectrum at each pixel in the data [9]. The acquired data is in the form of a so called "image cube" having two spatial dimensions (X and Y) and one spectral dimension (wavelength, λ) [10].

A hyperspectral imaging system basically consists of a broadband light source with the desired spectral band (including the wavelength band of interest) that focuses the light on the target, an electronically tunable filter to spectrally discriminate the reflected light from the target and a sensitive detector array (otherwise called a focal plane array), which collects this light and converts it into a two dimensional gray scaled image before transferring it into a computer for storage and analysis. An image at every desired wavelength is acquired over a period of time, thus forming a three dimensional image cube. [11]. Figure 2 shows an image cube formed by hyperspectral imaging.
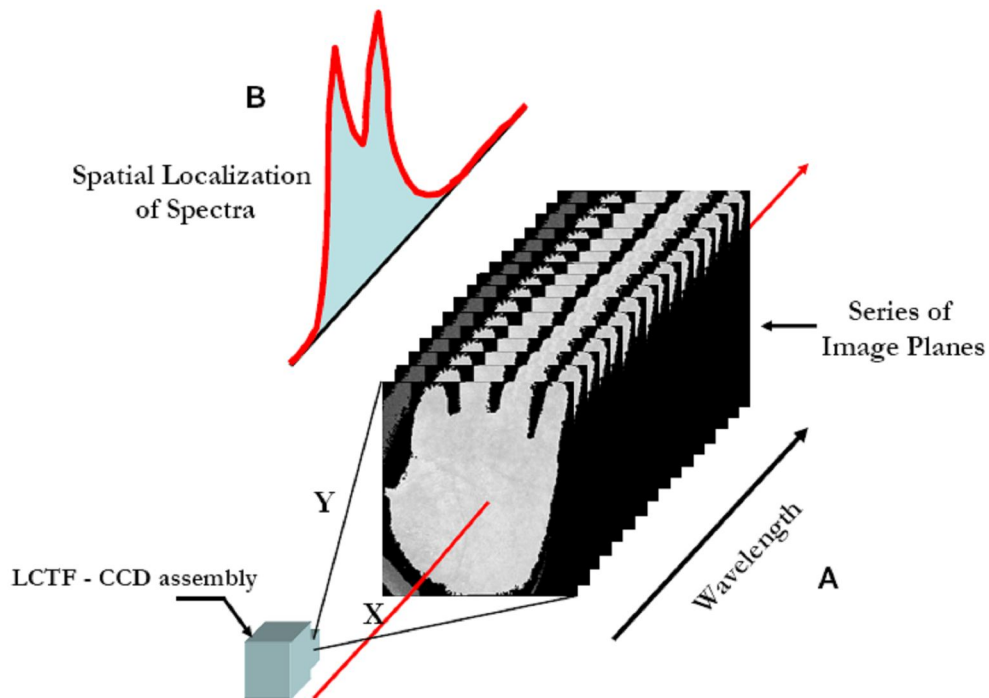
Figure 2. Hyperspectral Image Cube Visualization. A) Depicts sequence of images acquired at specific desired wavelengths. B) Depicts information obtained from each pixel within the hyperspectral image cube

The application of hyperspectral imaging in the biomedical field for determining the percent saturation of oxyhemoglobin perfusing the skin tissue was first demonstrated

by Zuzak et al. at the National Institutes of Health (NIH), Bethesda, Maryland [11, 12]. Improvements have since then been made to the existing prototype to develop a multimodal hyperspectral imaging system which enables surgeons to monitor amputation wounds over a period of time by determining the percent saturation of oxyhemoglobin accurately and precisely.

1.5 Components of the tissues

The tissues in the human body comprises majorly of oxyhemoglobin, de-oxyhemoglobin, lipids and water. Each of these components has inherent chromophores which help in spectrally distinguishing one from the other. For example, in vascular structures, those containing a higher amount of oxyhemoglobin can be differentiated from those containing higher deoxyhemoglobin level. This is the key factor that helps quantify the percent saturation of oxyhemoglobin. Oxyhemoglobin is an inherent blood chromophore formed during respiration and is predominant in red blood cells due to its bright red appearance. Deoxyhemoglobin, on the other hand, is an oxygen-unloaded chromophore which is purple blue in color [13]. Spectroscopic image data collected from an amputated region at each array detector is formatted into a three dimensional hyperspectral image cube. A deconvolution applied to the spatial and spectral information of this data cube based on reference spectra of pure oxyhemoglobin and pure deoxyhemoglobin (inherent chromophores), aids express the amount of oxyhemoglobin as a percent value. The images along with the percent value of oxyhemoglobin help the surgeon determine the perfusion of blood in the deeper and superficial tissues.

1.6 Research problem

The specific aim of this research is to utilize hyperspectral imaging technology to determine the ability to resolve the image details of an absorber at different depths and wavelengths spanning the visible to near-infrared, in an intralipid suspension modeling the human tissue. Real amputation data collected in the clinic is used to demonstrate that the multimodal hyperspectral imaging system is capable of non-invasively monitoring the *in vivo* blood perfusion in both the superficial and deep tissues in amputation wounds.

CHAPTER 2

METHODS

2.1 Instrument and components

The multimodal hyperspectral imaging system shown in figure 3 consists of two liquid crystal tunable filters (LCTFs), a radiometric power supply, a lamp source encased in housing, and focal plane arrays for both visible and near-infrared ranges. All these components are suitably mounted on a tripod manufactured by Quickset™. This system was developed in the Laboratory of Biomedical Imaging at the University of Texas at Arlington, based on its prototype developed at the National Institutes of Health, Bethesda. Each component of the system is explained in detail in the following sections.
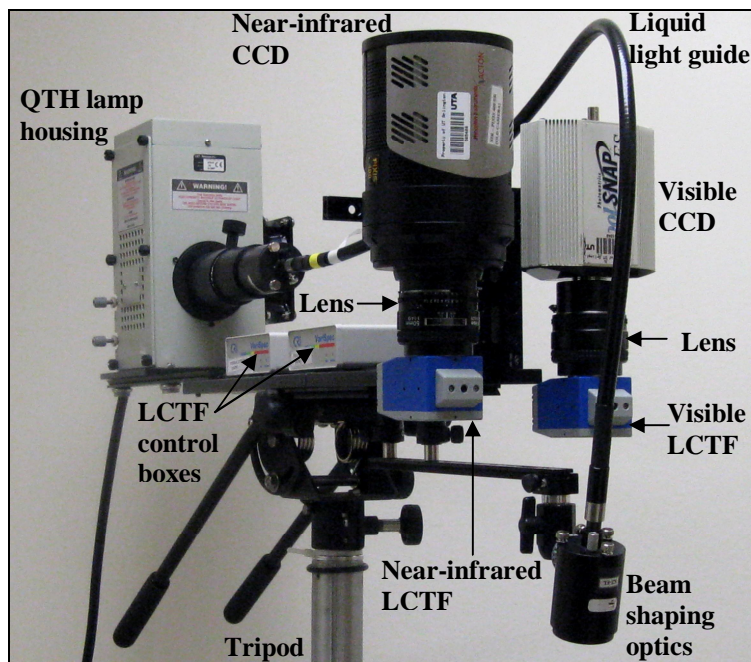
Figure 3. The multimodal hyperspectral imaging system

2.2 Liquid Crystal Tunable Filter (LCTF)

The diffused reflectance light from the imaged target passes through a Liquid Crystal Tunable Filter (VariSpec[TM] LCTF, Cambridge Research & Instrumentation (CRi), Woburn, MA). An LCTF behaves like a high-quality interference filter with the difference being that the wavelength range to be transmitted is electronically controlled, providing fast, accurate and vibration free selection of the wavelength [14].

Figure 4. LCTF module comprising of the LCTF and the control box [15]

The LCTF along with its control box is shown in figure 4. It has solid-state construction, with no moving parts and vibrations, and works by applying voltage to its liquid crystal elements, to select a particular wavelength range to be transmitted, while blocking the rest of the wavelengths. There is a feedback circuit associated with the LCTF, which grants it a stable and precise wavelength tuning continuously over hundreds of nanometers that is independent of ambient temperature in the range of 10°C to 40°C [15, 16].

Liquid-crystal tunable filter works on two principles: birefringence and polarization. It is essentially a multistage Lyot-Ohman type interference filter, but with a liquid crystal waveplate in each stage providing an electronically controllable variable retardance. A schematic of a single stage LCTF is shown in figure 5. The linearly polarized light passes through the birefringent element (fixed retarder), rotated 45° with respect to linear polarizer, where it experiences an optical path difference depending on the birefringence of the materials, the material thickness and the incident wavelength itself [17 - 19].

After the light exits through the fixed retarder, it passes through the liquid crystal waveplate and finally through the linear polarizer. The last linear polarizer is oriented parallel to the input linear polarizer. The electronically controlled waveplate is made up of combination of liquid crystal plate and a quartz plate, hence the name liquid crystal tunable filter. The liquid crystal waveplate consists of two transparent electrodes (indium-tin oxide) on both sides of a cell containing liquid crystals that are initially aligned with their long axis nearly perpendicular to the light path.
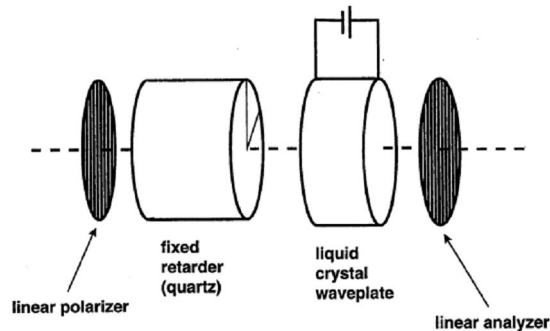
Figure 5. Schematic of a LCTF stage [19]

The inner surfaces of the cell are prepared in such a way that the molecules have a preferred orientation parallel to the surface. However, this orientation changes when an

E-field parallel to the light path, twisting the direction of liquid crystal into the direction of the E-field appears. The twist of the liquid crystal in response to the E-field is proportional to the strength of the applied field. The resulting orientation of the molecules causes the retardance to change, producing a wave plate with an electronically adjustable retardance [17 - 19]. Figure 6 shows the schematic representation of the liquid crystal in the presence of electric field.
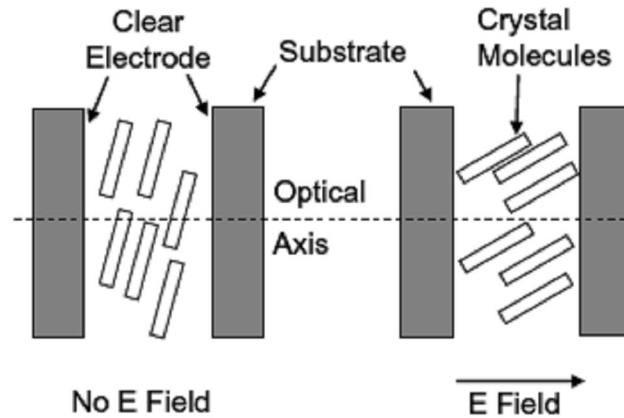
Figure 6. Schematic representation of alignment of liquid crystal in the presence of electric field [20]

The light finally passes through the exiting linear polarizer, oriented parallel to incident linear polarizer and transmits wavelengths that have undergone an integral phase shift. To isolate a single wavelength λ, multiple retardance stages are needed. These subsequent stages are placed in series with the retardance of each cell increased by a factor of 2. The transmittance through the LCTF is hence dependent on the integrated phase shift, which, in turn depends on the combined retardance. The polarizers between successive retarders offer better spectral control, with the trade-off being the transmittance through the LCTF. Each polarizer introduces a transmission loss of about 5%, resulting in an overall transmission loss of 50 – 70% [15 - 17], but if the light

entering the incident polarizer is polarized, the transmission is increased by a factor of 2 as compared to randomly polarized light [15].

The spectral range of the LCTF is determined by the first stage of the filter which has the thinnest birefringent element and the band pass is determined by the last stage which has the thickest element [19].

The LCTF module as shown in figure 4 consists of the filter (optics module) and the control box (electronics module). The host computer communicates through a hyperterminal and ASCII commands with the electronics module. The desired pass band wavelength is fed to the electronics module, which calculates the required drive level (voltage) for each tunable element in the optics module [15, 21].

The response time for switching from one wavelength to another depends on various factors like liquid crystal relaxation time from "charge" to "no charge" state under various ambient temperatures and the calculation of the electronics controller box, which must send the correct voltages to each LC element for each change. Typically, the response time is between 50 to 150 ms.

Some of the important specifications for the near-infrared low resolution and visible low resolution LCTFs used in this project are tabulated in table 1.

2.2.1 LCTF Operating Considerations

Some of the operating considerations for working of LCTF are discussed below.

2.2.1.1 Variation of FWHM with pass wavelength

The bandwidth is defined as full-width at half-maximum (FWHM) of the transmission curve, i.e., the number of adjacent wavelengths transmitted at FWHM, in addition to the tuned wavelength. The FWHM is constant for Lyot filters and varies as

1/8 of the wavelength. The bandwidth is fixed for LCTF and cannot be adjusted in the field [21].

Table 1. Specifications for the NIR and visible low resolution LCTFs

Parameters	Varispec^{TM} NIR LCTF	Varispec^{TM} Visible LCTF
Clear aperture	20 mm	20 mm
Bandwidth (FWHM)	4.5 – 12.5 nm	6 – 16 nm
Field of View (half-angle)	± 7.5° from normal	± 7.5° from normal
Wavelength range	650 – 1100 nm	400 – 720 nm
Wavelength accuracy	Bandwidth / 8 ± 0.5 mm	Bandwidth / 8 ± 0.5 mm
Optics response time	150 ms	50 ms
Operating temperature	10° - 40° C	10° - 40° C

2.2.1.2 Response time versus tuning wavelength

There is no simple relationship between the response time to change from one wavelength to another and the wavelength involved, hence some wavelength requests tune more LC elements than other ones, resulting in shorter or longer tuning speed [21].

2.2.1.3 Response time versus temperature

The liquid crystal variable retarders set the response time of the filter, and their viscosity varies with the temperature. High temperature (30° – 35° C) is preferable for LCTF working as it reduces the response time. If the optics temperature is cooler than 20° C, response time is longer than that given in the table 1 [21].

2.2.1.4 Thermal drift and re-initialization

The Varispec^{TM} filter exhibits slight drift when the optics module temperature changes, resulting in a slight wavelength error, but performing the initialization routine

renders the filter insensitive to temperature and reduces this error significantly. If the ambient temperature changes by more than $\pm\, 3^{\circ}$C, it is wise to re-initialize the filter [21].

2.3 Camera lens

The spectrally discriminated images produced by the LCTF are focused onto the CCD camera detector with the help of a 50mm f/1.4D AF lens manufactured by Nikon. It is a fast lens suitable for shooting in any type of light. The images produced are distortion free and have very good resolution and color rendition [22]. This lens serves as an ideal first lens, perfect for any type of available-light shooting [22]. The lens is shown in figure 7.

Figure 7. A 50mm f /1.4D AF Nikon lens

There are a number of F-stops for this lens, which can accordingly be used to expose the camera CCD. A ring present on the front side of the lens can be used to adjust the focus on the image and the back side fits into a C-F mount which can be used to couple the camera with the variable focus lens. This lens has excellent spectral response in the visible region, as shown in figure 8.
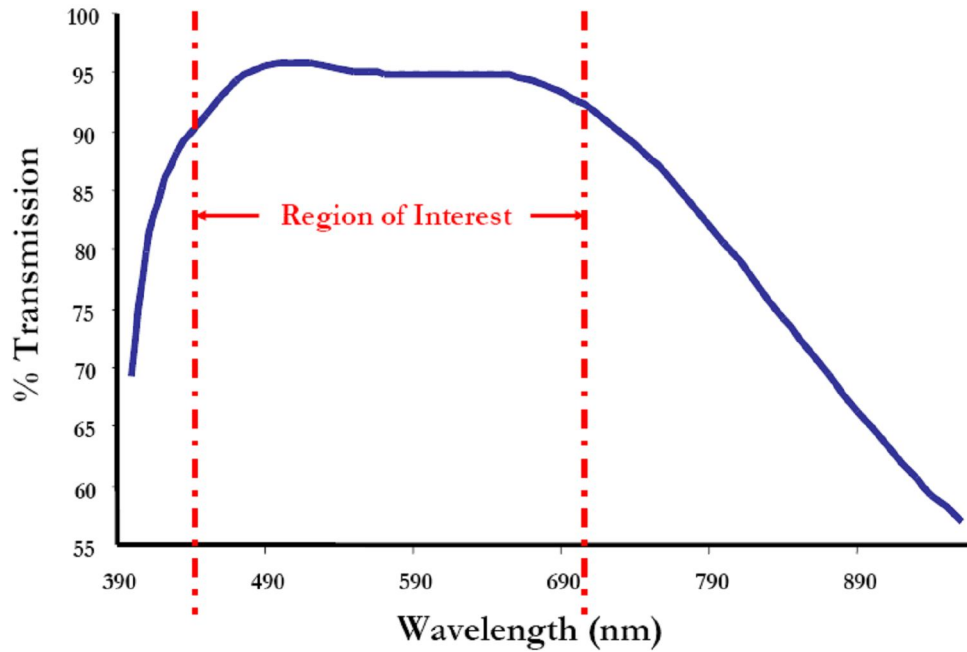
Figure 8. Spectral response of the Nikon 50mm f/1.4D AF lens

From the figure, it can be clearly seen that the response in the visible region is relatively flat, which minimizes the noise introduced by the lens.

2.4 Focal Plane Array (FPA)

The Charge Coupled Device (CCD) or FPA primarily converts an incoming photon of light to an electron, thereby generating a charge. In addition to charge generation, the CCD accumulates and stores the charge, and transfers them when they are ready for read out. They can roughly be thought of as two-dimensional grid of individual photodiodes (pixels), each connected to its own charge storage "well". The intensity of light falling on the collection area of each pixel is sensed and a proportional amount of charge is stored in the associated "well". Once charge accumulates for the specified exposure time, controlled through software, the pixels are read out serially [23].

2.4.1 PIXIS 400BR near-infrared camera

        The focal plane array used for the near-infrared region application in this experiment is a PIXIS 400BR from Princeton Instruments (PI Acton, Tucson, Arizona). The PIXIS 400BR is a fully integrated system with permanent vacuum/deep cooling. It uses a high performance spectroscopic-format CCD designed exclusively for Princeton Instruments/Acton [24]. It is designed for low light level spectroscopy applications. The temperature range for optimal operating characteristics for this CCD is 5° C to 30° C. Generally, lowering the temperature of the FPA enhances the quality of the acquired signal. The specifications for the PIXIS 400BR camera are given in Table 2, and figure 9 shows the camera.

Figure 9. PIXIS 400BR Focal Plane Array

Table 2. Specifications of the PIXIS 400BR camera

Specifications	
CCD format	1340 x 400 imaging array 20 x 20 μm pixels 26 x 8 mm imaging area
Well capacity	300 Ke-, High Sensitivity mode 1 Me-, High capacity mode
System read noise	5 e- rms @ 100 KHz (maximum) 16 e- rms @ 20 MHz (maximum)
Non-linearity	< 1% @ 100 KHz, < 2% @ 2 MHz
Dynamic range	16 bits
Frame readout	35 Hz @ 100 KHz digitization 74 Hz @ 2 MHz digitization
Deepest cooling temperature	-70º C (High sensitivity mode) -75º C (High Capacity mode)
Dark current @ -75 ºC operation	0.5 e-/p/s
Thermoelectric precision	± 0.05º C over the entire temperature range
Operating environment	5º C to 30º C non-condensing

PIXIS 400BR camera has controlling software which controls the temperature and maintains it within ± 0.05º C of the set temperature by controlling the camera's cooling circuits [23]. Dark charge is the thermally induced buildup of charge in the FPA over time. The statistical noise associated with this charge is known as dark noise. With the

light into the camera completely blocked, the FPA will collect a dark charge pattern, depending on the exposure time and the camera temperature. The longer the exposure time and the warmer the camera, the larger and less uniform the background will appear [23].

PIXIS 400BR camera incorporates dual digitization (100 KHz/2 MHz), which means that there is a choice of how quickly the data will be digitized. The 2 MHz conversion speed is used for the fastest possible data collection and 100 KHz conversion speed is used where the noise performance is the primary concern [23, 24].

Controller gain is software selectable and can have three states 1 (low), 2 (medium) and 3 (high). Low gain allows digitization of larger signals, medium is suitable for mid-level intensity signal whereas high gain allows low level signal measurement [23].

Megapixel resolution and small pixels allow imaging of very fine details, yet the pixels can be easily binned to improve sensitivity. The resolution is further enhanced by employing a 1340 x 400 imaging array. The shuttering provided in this camera eliminates camera vibration and the ability to select the bin setting increases light sensitivity, thereby increasing the frame rate. The most prominent advantage of this camera system is that it has a 16-bit digitizer that allows the bright and dim signals to be quantified in a single image [23, 24].

The spectral response of the camera shown in figure 10 points out that the quantum efficiency is maximum (88%) within the wavelength region of interest, 650 nm to 1050 nm used for data collection in this study and it never drops below 20%. The PIXIS 400BR is a back illuminated CCD, allowing the light to be collected through the

back surface. The surface of the back illuminated CCD is etched to 15 - 30 μm thickness in order to collect light through the back surface. As a result of this modification, no light is lost through absorption and reflection, giving these CCDs twice the quantum efficiency of their front-illuminated counterparts. However this process makes them semi-transparent in the NIR region, reflections between front and back surfaces causing them to be partial etalon. This unwanted etalon-like behavior creates spectral as well as spatial etaloning in back illuminated CCDs. To minimize etaloning, the PIXIS 400BR is made of thicker silicon, roughly double the thickness of a normal back-illuminated CCD contributing to absorption of NIR light minimizing interference with increasing QE.
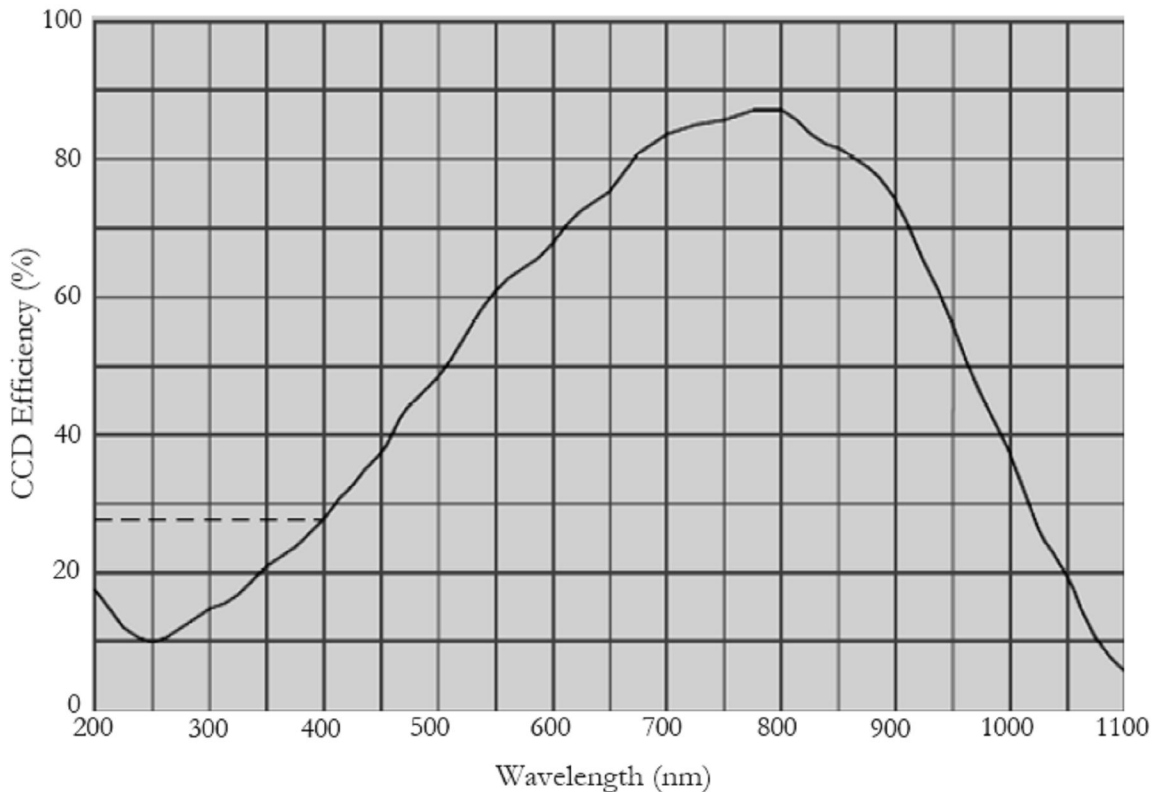
Figure 10. Spectral response of the PIXIS 400BR FPA adopted from Photometrics Inc.

The anti-reflective coating has been optimized for NIR wavelengths, reducing the amount of light reflected into the CCD when the light returns to the back surface of the

CCD from the polysilicon side. The CCD back surface is processed in a proprietary manner that helps to break up the etalon effect [24, 25].

2.4.2 CoolSNAP$_{ES}$ visible camera

The CoolSNAP$_{ES}$ manufactured by Princeton Instruments Inc. (formerly Roper Scientific), is a scientific grade fast digitizing CCD used to acquire the hyperspectral data in the visible spectrum of light for this experiment. This camera is optimized for moderate to low-light level applications that demand both high speed and high spatial resolution. The major specifications for CoolSNAP$_{ES}$ are given in table 3.

Table 3. Specifications of the CoolSNAP$_{ES}$ camera

Specifications	
CCD format	1392 x 1040 imaging array
	6.45 x 6.45- μm pixels
	8.77 x 6.6-mm imaging area (optically centered)
Well capacity	16,000 e- (single pixel)
	30,000 e- (2 x 2 binned pixel)
System read noise	< 8 e- rms @ 20 MHz
Non-linearity	< 1%
Dynamic range	12 bits @ 20 MHz
Frame readout	91 ms / frames
Cooling	Thermoelectric, 50º C below ambient temperature
Dark current	1 e-/p/s
Operating environment	15º C to 30º C ambient
Dimensions	4.5" x 5.0" x 2.5" (1.9 lbs)

The CoolSNAP$_{ES}$ monochrome camera shown in figure 11, incorporates a SONY ICX-285 silicon chip with Interline-transfer capability [26]. Interline-transfer CCD takes a structure such that the column of photo-sensing sites (so called "pixels") and vertical registers are arrayed alternately. The pixels convert the incoming light into electrical charge over a 1/60-sec period. After this period, the accumulated charges are transferred to the vertical shift registers during the vertical blanking period. The charges within the same line (the same row in the CCD array) are then shifted down through the vertical shift register in the same sequence and read into the horizontal register, line-by-line [27]. Figure 12 shows the process of interline transfer.

Figure 11. CoolSNAP$_{ES}$ CCD camera
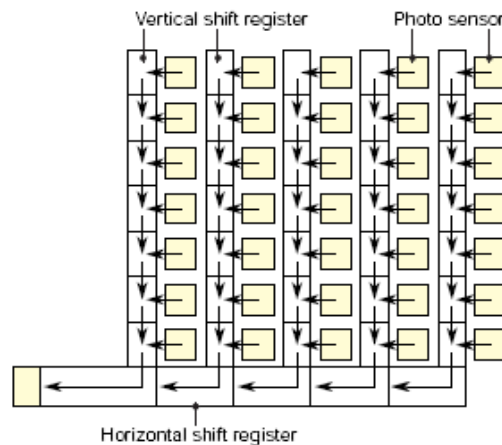
Figure 12. CCD interline transfer

The major drawback of interline transfer CCDs is their poor sensitivity to photons due the opaque mask covering a large portion of each pixel [28]. To improve photon sensitivity, on-chip lens technology is used in high quality interline transfer devices, that enhances light collecting capability. The micro-lens above each pixel effectively directs the light to them [27].

The SONY ICX-285 silicon chip is equipped with another key feature called anti-blooming capability. Blooming is the migration of charges from one pixel to its adjacent pixel. The chip has the capability to remove the excess of charge generated from an overexposed pixel to the "drains", built within the CCD [27].

The electronic shuttering provided in this camera eliminates camera vibration and the ability to bin the camera increases signal to noise ratio while increasing the frame rate. The CoolSNAP$_{ES}$ has a 20 MHz digitizer built into it and hence provides a high speed and high sensitivity readout over a high-resolution 1329 x 1040 imaging array [29].
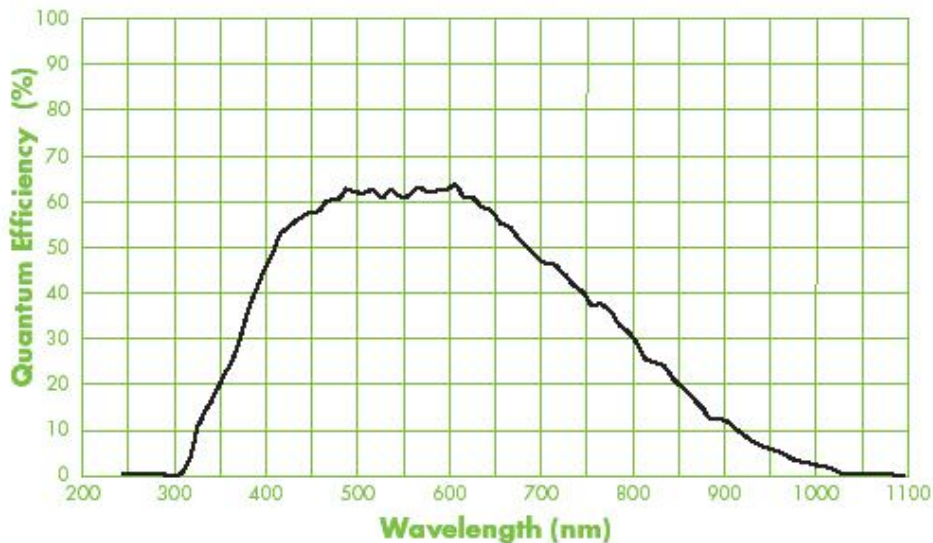
Figure 13. Spectral response of CoolSNAP$_{ES}$ CCD adopted from Photometrics Inc.

The quantum efficiency (QE) of this camera is above 60% in the region of interest i. e., between 500 – 650 nm and it is constant for this range of wavelengths. The spectral response of the CoolSNAP$_{ES}$ camera is shown in figure 13.

Apart from the characteristics mentioned above, CoolSNAP$_{ES}$ CCD has four different bin settings: 1 x 1, 2 x 2, 3 x 3 and 4 x 4. A higher bin setting brings down the exposure time for the experiment and requires less storage area with the trade-off being the spatial resolution. A higher bin setting reduces the spatial resolution. Technically, binning, as shown in figure 14, is the process of adding the data from adjacent pixels together to form a single pixel (a super pixel), and binning can be accomplished either through hardware or software [29].
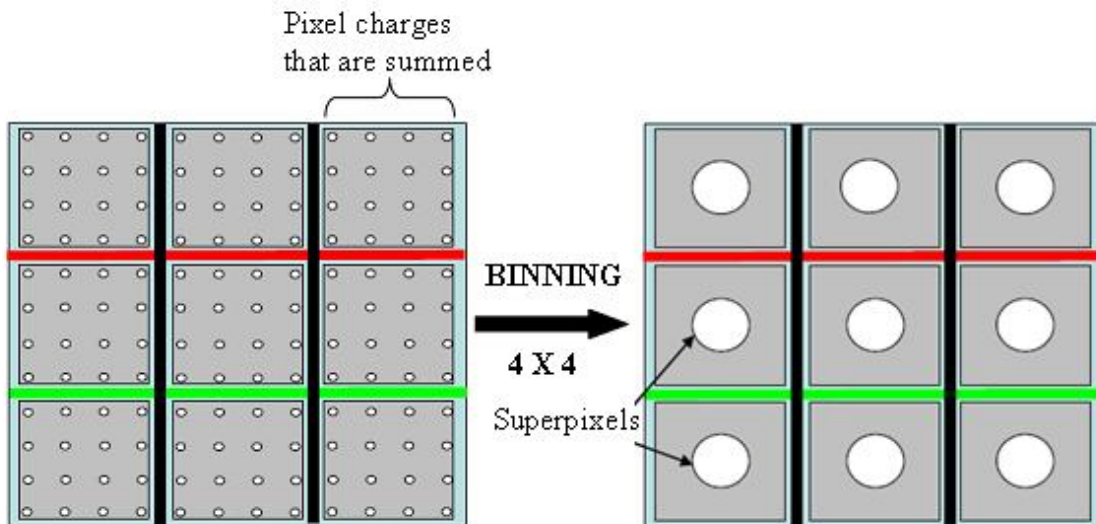
Figure 14. Formation of a super pixel from summation of 16 pixels, hardware binning 4 x 4 [29]

Hardware binning is performed on the CCD array before the signal is read out of the output amplifier. Here adjacent pixels are transferred into the serial registers at a time and from there, into the summing well. Finally, the pixels are summed up and shown as a single pixel in the final image. If the CCD has 12 µm pixels, then 2 x 2 binning will yield

an effective pixel size of 24 µm. Similarly, 3 x 3 binning will yield an effective pixel size of 36 µm and 48 µm if the binning is 4 x 4 [30].

A limitation of hardware binning is saturation, the point at which a pixel, the serial register or the summing well reaches its maximum capacity. When saturation occurs, any charge beyond the saturation value will be truncated and the final image will reflect the maximum pixel value rather than the actual value. The charge spilling also reduces the contrast [30]. The solution to this problem is software binning. However, software binning is not as fast as hardware binning.

The CCDs explained above which are used in this experiment are driven by PVCAM software, which stands for Photometrics Virtual Camera Access Method. PVCAM is a set of library routines that implements a camera's operation in a hardware-independent, platform-independent ("virtual") suite of function calls. The programming for setting up the experimental parameters like exposure time, binning, region of interest, and CCD gain, is done in Vpascal, which is integrated in V++. V++ is precision digital image processing and enhancement software and controls any PVCAM-compatible feature. The whole process of data acquisition is automated through V++ [31, 32].

2.5 Radiometric power supply and source

A Quartz Tungsten Halogen (QTH) lamp source along with a power supply that drives a constant current through it is used as a broad band light source in the experiment. QTH lamps are popular visible and near-infrared sources because of their smooth spectral curve and stable output. They do not have the sharp spectral peaks that arc lamps exhibit, and they emit little UV radiation [34]. The QTH source and the power supply come from

Spectra-Physics, a division of Newport Corporation. Figure 15 shows the QTH lamp housing (model 67010) that houses the 250 watt QTH lamp source (model 6334) and the radiometric power supply (model 69931), used in this experiment.

Figure 15. QTH lamp source and the radiometric power supply

The Oriel radiometric power supply is a highly regulated source of constant current or constant power for QTH lamps. This power supply has some important features like reliability, small size, ease of use and economical price. There is a power ON/OFF button along with adjustments for current/power preset and limit. It also has provisions for monitoring the current, voltage, power and operating time. The specifications of this power supply are given in table 4.

In this experiment, the power supply is run on constant current mode in which a current of 10.42 Amperes is driven through the QTH lamp source. The QTH lamp housing manufactured by Oriel provides a safe enclosure for QTH lamps [35]. It holds the ignitor, condensing optics, rear reflector and lamp cooling fan [33]. Condensing optics produce large collimated beams collimated by full line of optical accessories [35]. Each condenser assembly consists of a lens element(s) inside the barrel housing with a locking focusing lever. These condensers are designed to produce a collimated beam, but

the focusing lever lets the user adjust the lens position to produce a converging or diverging beam [33]. The rear reflector provided in the lamp housing captures radiations which are emitted backwards, and when properly adjusted, reflects it back to the source to contribute to the total output [35]. Re-imaging onto the filament does increase the collimated output a little and changes the power balance of the system [36].

Table 4. Specifications of the radiometric power supply

Parameters	Values for model 69931
Input voltage	90 - 264 VAC
Input current	5 A
Input frequency	47 - 63 Hz
Output power	40 - 300 W
Output current	0 - 15 A
Output voltage range	0 - 45 VDC
Meter accuracy (% of full scale)	< 0.05 %
Digital meter resolution, voltage	0.1 VDC
Digital meter resolution, current	0.01 A
Digital meter resolution, power	1 W
Operating mode	Constant current or constant power
Ambient operating temperature	0 - 45 °C
Weight	20 lb (9 kg)

The convectively cooled housing also has a built-in fan with power sense, which allows the operation of the fan from 10 – 250 watts. The housing as well has safety

features to prevent lamp damage and accidental exposure. A door interlock prohibits the operation of the lamp while the door is open; a temperature sensor monitors the lamp's operating temperature and controls the cooling fan accordingly. The reason for choosing the 250 watt QTH lamp from Oriel is its excellent spectral response over the spectral region of our interest (from 400 nm to 800 nm).
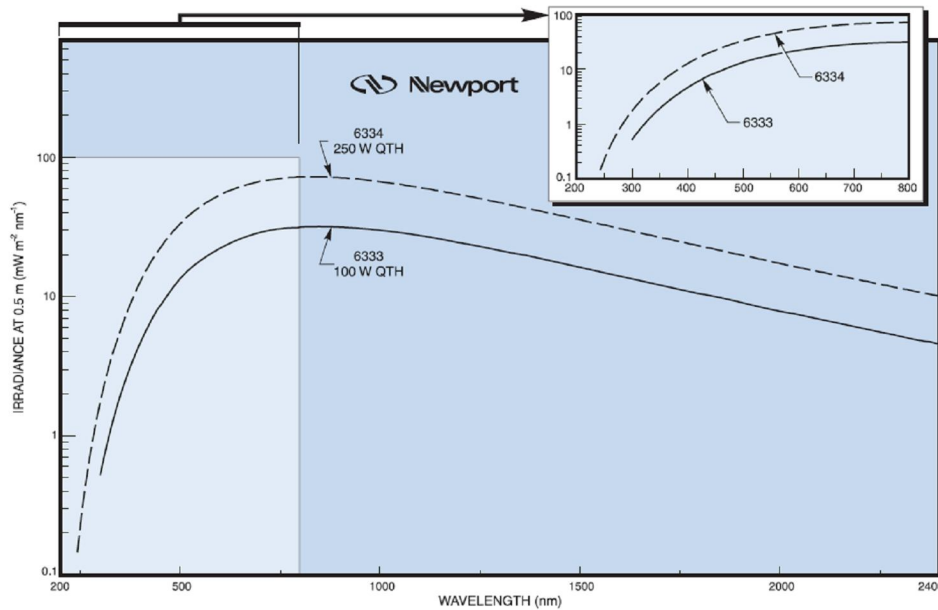
Figure 16. The spectral irradiance of the 250 watt QTH lamp source [37]

The spectral irradiance of the 250 watt QTH lamp source in comparison with the 100 watt QTH lamp source at a distance of 0.5 meters from the target is shown in figure 16. The spectra are provided by Newport Corporation. It can be clearly noticed that there is an increase in the spectral irradiance for the 250 watt lamp, compared to the 100 watt lamp.

The power density measured at a distance of 0.56 meters from the source is 4.7 w/m^2. This value falls in the safe range for exposure of human skin to light, which is 10 w/m^2. Thus it can be seen that there is a greater output of photons from a 250 watt lamp

source as compared to the 100 watt source, which can be attributed to a greater wattage

of the former.

CHAPTER 3

EXPERIMENTAL SECTION

3.1 Reference Spectra

The reference spectra for pure oxyhemoglobin (HbO$_2$) and pure deoxyhemoglobin (Hb) are required to estimate the percent contribution of both these components in the tissues by the method of deconvolution of the hyperspectral data. A multivariate least square algorithm is used to calculate the spatially distributed oxyhemoglobin concentration. The reference spectra for oxyhemoglobin and deoxyhemoglobin were obtained from pure HbO$_2$ and Hb solutions prepared at the National Institutes of Health (NIH) by standard methods from blood collected from a healthy, non-smoking individual, using the original system developed at NIH for the visible and the near-infrared regions. Two regions of interest, 520 – 645 nm and 650 – 1050 nm in visible and near-infrared respectively, containing the peaks of oxy and deoxyhemoglobin were selected for image imaging and analysis. The reference spectra for the visible region are shown in figure 17 and that for the near-infrared region in figure 18.
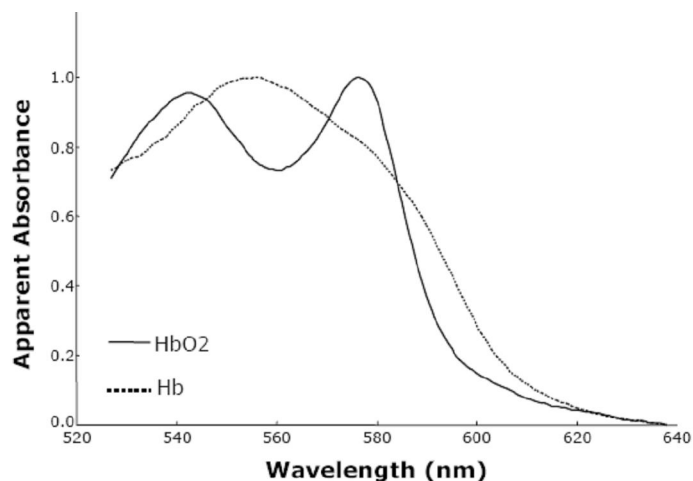
Figure 17. Reference spectra for oxyhemoglobin and deoxyhemoglobin in the visible region [11]
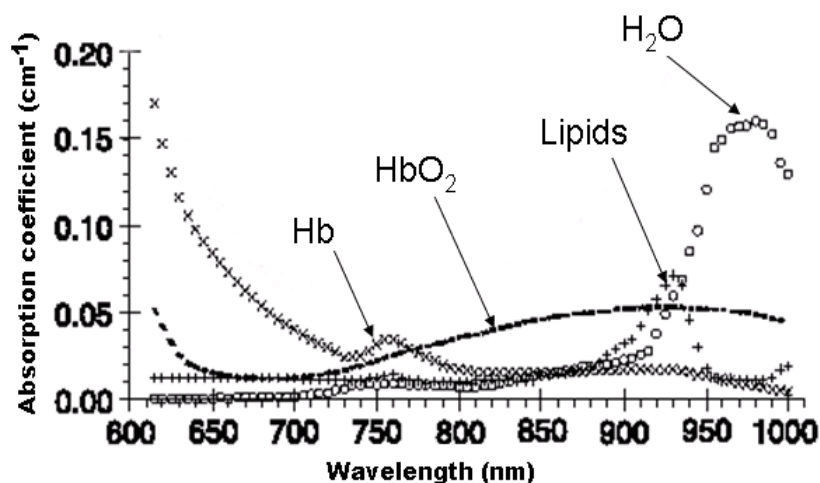
Figure 18. Reference spectra for oxyhemoglobin, deoxyhemoglobin, lipids and water in the near-infrared region [45]

3.2 Intralipid^{TM} 20%

Intralipid 20% (a 20% intravenous fat emulsion) is a sterile, non-pyrogenic fat emulsion prepared for intravenous administration as a source of calories and essential fatty acids, manufactured by Fresenius Kabi, Uppsala, Sweden. It is made up of 20% soybean oil, 1.2% egg yolk phospholipids, 2.25% glycerin, and water for injection. In

addition to this, sodium hydroxide is added to adjust the pH so that the final pH of the product is 8 (6 – 8.9 range) [38].

It is known that intralipid 20% diluted with distilled water, down to a concentration of 1% mimics the properties of tissue reasonably well. Distilled water is used since it prevents unwanted impurities and scattering effects [5, 6, 7].

3.3 Bombay blue India ink

India ink is considered to be a good absorber and can be used with an aqueous solution of intralipid (described above) to produce a popular phantom that reproduces the optical properties of biological tissues, in terms of absorption and scattering coefficients [7, 8]. Blue india ink is used as absorber in this experiment.

3.4 Experiment protocol

A proof of principle clinical study was performed to demonstrate the application of the multimodal hyperspectral imaging system to monitor the perfusion of blood in amputation wounds. The experiment involved data collection done at the Veterans Affairs Hospital, Dallas, under the supervision of Dr. Karel J. Zuzak, Ph. D., after receiving approval from the Institutional Review Board (IRB), and analysis of this data at the Laboratory of Biomedical Imaging (LBI), Department of Bioengineering, University of Texas at Arlington. Modeling and imaging of the tissue phantom was also done at LBI.

3.5 Experimental parameters

The parameters like wavelengths for the LCTFs, exposure time, binning and gain for both cameras are determined for optimized data collection. There is always a trade-off between the data acquisition time and the quality of the images.

For the near-infrared region, the wavelength range selected was 650 – 1050 nm in increments of 5 nm. This particular region is selected due to the fact that the PIXIS 400BR camera has the greatest quantum efficiency in this region. It tends to yield noisy data if the quantum efficiency falls below 10%. Moreover, this region is ideal for obtaining distinct oxyhemoglobin and deoxyhemoglobin spectral information. The LCTFs contain a palette of 128 distinct registers that store voltages associated with the desired wavelengths which are determined prior to acquisition. For the selected region of 650 – 1050 nm, increments of 5 nm produces a total of 81 wavelengths. An increase in the exposure time is effected if the LCTF is to store more than 128 wavelengths, due to re-initialization after the first 128 wavelengths. Due to this it is always desirable to keep the total number of wavelengths below 128.

The spectral output of the system is obtained by placing a spectralon reflectance material, which is considered to have the highest diffuse reflectance of any known material or coating over the UV – VIS – NIR region of the spectrum [39], in the light path and collecting a hyperspectral image cube. This data cube is used for generating the spectrum, by using a Matlab script. It can be seen from the spectral output shown in figure 19, plotted with the LCTF on and using the spectralon that the transmittance of the near-infrared system is wavelength dependent.
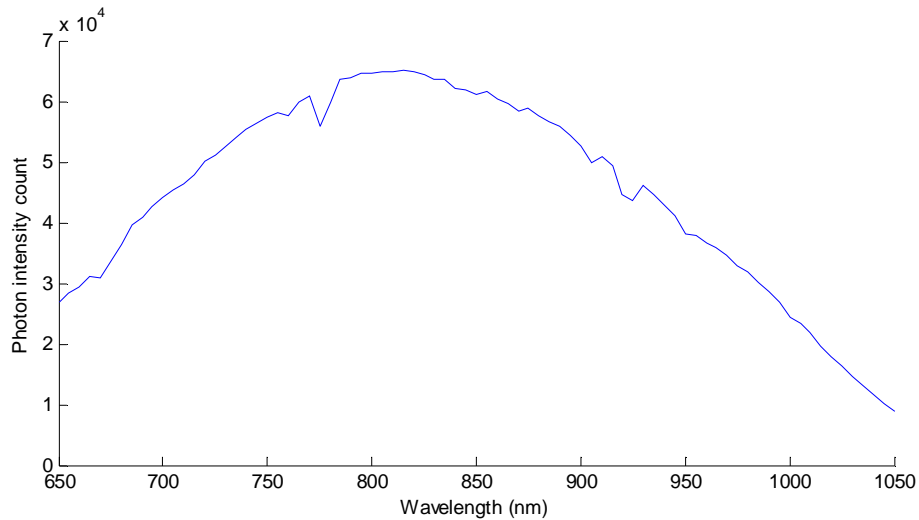
Figure 19. LCTF-FPA combined spectral output of the near-infrared camera

The lens of the near-infrared camera is set to the smallest F-stop, for maximal light allowance to the FPA and the LCTF is tuned to 750 nm. The FPA consisting of a 16 bit analog to digital converter gives a maximum count of 65,535 (2^{16}), reached by the pixels. In order to be assured that the CCD does not get saturated while imaging, the spectralon, as explained above is placed in the light path and the reflected light from its surface is captured by the camera and displayed in image format by means of V++ software from Digital Optics. The maximum intensity counts should be optimally between 61,000 and 62,000 and the corresponding exposure time, depending on the imaging conditions generally ranges from 8 – 15 ms.

32
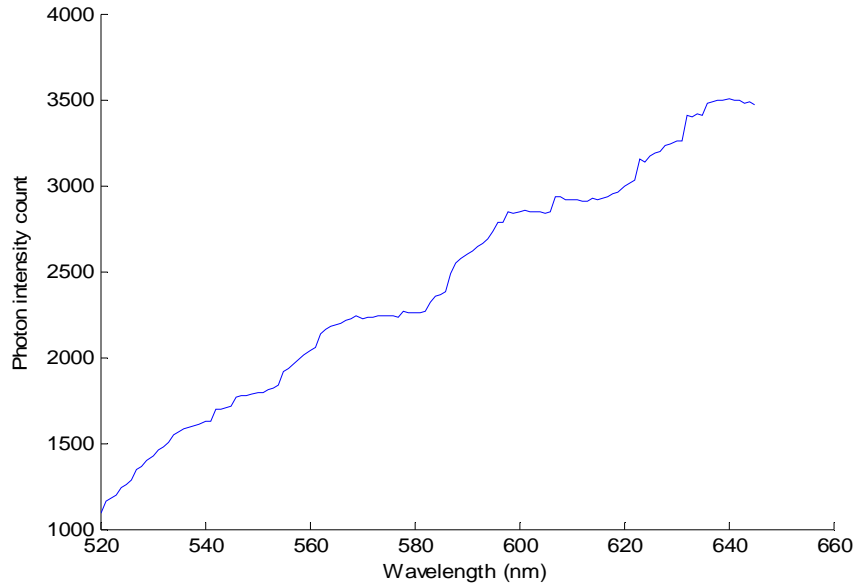
Figure 20. LCTF-FPA combined spectral output of the visible camera collected using spectralon

The wavelength range of interest selected for the visible region is 520 – 645 nm in increments of 1 nm constituting 126 wavelengths, due to the high quantum efficiency in this region as can be seen from figure 20. The CoolSNAP$_{ES}$ camera used in the visible region has a 20 MHz, 12 bit digitizer, which increases the frame readout, thereby reducing the exposure time to nearly half as compared to the PIXIS 400BR. The maximum photon count reached by the CCD is 4095, because of the 12 bit digitizer. The visible LCTF is tuned to 645 nm owing to the highest transmittance at this wavelength, found by placing a spectralon surface in the light path. The exposure time for the visible camera is also experimentally determined in the same way as that for near-infrared camera. It typically falls in the range of 4 – 8 ms. As a buffer, the exposure time is determined for a maximum intensity count of 3500.

3.6 Modeling using the intralipid phantom

3.6.1 Preparation of the model

In the modeling experiment, intralipid 20% is diluted down to a concentration of 1% using distilled water to make a suspension, and blue india ink is filled in a capillary tube 150 mm long with 2.9 – 3.05 mm outer diameter and 1.5 – 1.6 mm bore (inner diameter). The ink capillary is fixed onto a plastic holder attached to a vernier height gage capable of measuring vertical movements with a precision of 0.02 mm.

The intralipid suspension is filled to the brim of a plastic tub till it overflows into a bigger tub, in which the small one holding the suspension is placed. Using the capillary holder and the height gage, the capillary is positioned at the surface of the suspension, such that half the tube diameter-wise, is immersed in it. The reading on the vernier scale with the ink capillary at this position is noted. This is the initial position of the capillary, from where the depth is determined. The tripod with the cameras mounted is moved to focus on the tub with the suspension and the ink capillary. The intralipid phantom is illuminated with a broad band light, such that a ring of light with the ink capillary at the center forms. The maximum intensity counts on both the cameras are set to the value ranges mentioned earlier and the foci of both the cameras are varied independently using the lenses attached to bring the ink capillary in the best possible focus. The distance between the lamp source and the target (surface of the intralipid suspension) is set at 22 inches. Figure 21 shows the experimental set up used in the imaging mode, for acquiring the intralipid model data.

Figure 21. Experimental set up of the multimodal hyperspectral imager for acquiring images of the intralipid phantom model

Figure 22 depicts the top view of the experimental set up to demonstrate how the cameras are simultaneously focused on the phantom model, and has the parts labeled in it.

3.6.2 Data acquisition

3.6.2.1 Intralipid model data

Two Dell^{TM} Latitude 620 laptops, one for setting the visible camera parameters and the other for near-infrared, are used in this experiment. The parameters like LCTF wavelength range, bin, exposure time, tune wait time, image size, and CCD gain are determined prior to acquiring the data and fed into both the laptops, using V++ software.

A V++ script written for data acquisition in the visible and near-infrared cameras is run for collecting hyperspectral image cubes in both ranges, for the initial position of the ink capillary in the suspension.
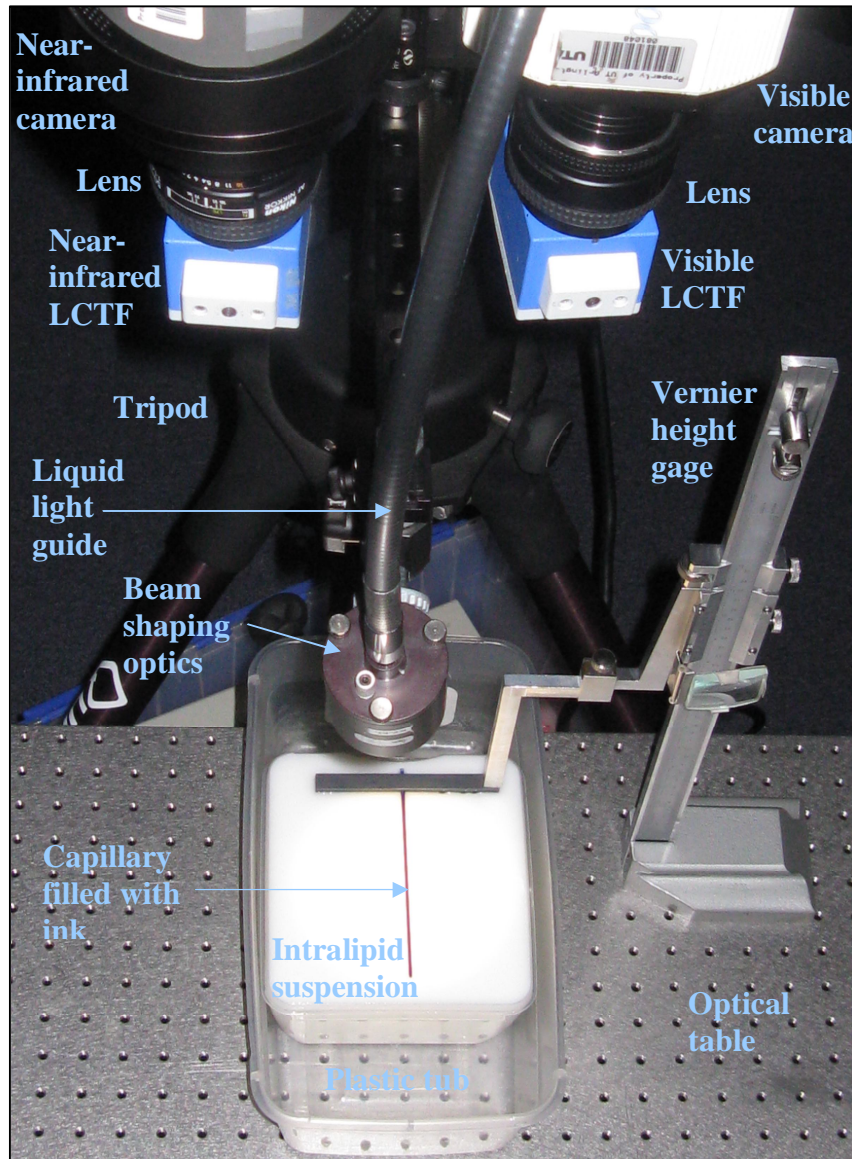
Figure 22. Focusing the cameras on the phantom

The level of the capillary tube is then brought down by a millimeter into the suspension, using the vernier scale. The tub is again filled to the brim with the suspension to make sure that the surface level of the intralipid from which depth of the capillary is

measured is the same every time. Now the capillary is 1 mm below the reference point. A data cube is again acquired for this depth. This process is repeated for every millimeter (up to 35 mm in this case) the capillary is immersed into the suspension, and the image data acquired by both the cameras are stored in *.dat format in the respective laptops.

The V++ script controls the LCTF and the camera simultaneously. The block diagram of the experimental set up for the visible/near-infrared hyperspectral imaging system is shown in figure 23.

```
┌──────────┐          ┌──────────────┐
│ Computer │◄·········│     FPA      │
└──────────┘          │ CoolSNAP/PIXIS│
                      └──────────────┘
                             ▲
                      ┌──────────────┐
                      │    50 mm     │
                      │  Nikon lens  │
                      └──────────────┘
                             ▲
                      ┌──────────────┐
                      │     LCTF     │
                      │ (Visible/NIR)│
                      └──────────────┘
          ┌──────────────┐    ▲
          │ Illumination │    │
          │    source    │  Path of light
          └──────────────┘
                      ┌──────────────┐
                      │ Target/Subject│
                      └──────────────┘
```
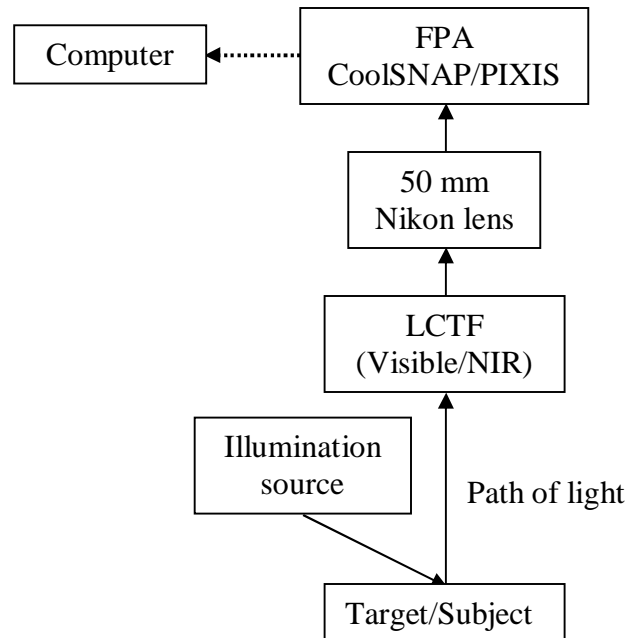
Figure 23. Block diagram of the experimental set up

After the data collection is over, the tub containing the intralipid suspension is removed and a spectralon reflectance material is placed at the level at which the brim of the intralipid tub (surface of the suspension) was. The reflectance of the spectralon is generally >99% over a range from 400 to 1500 nm [39]. The spectralon is illuminated with the broad band light and the exposure time and aperture of both the cameras are adjusted so as to keep the reflected photon counts at ~90 – 95% of the maximum. This is

done so as to make certain that the CCDs do not saturate. The foci of both the cameras are adjusted and an image cube is acquired. This data cube is used for finding the apparent absorbance of the ink, by ratioing.

3.6.2.2 Amputation data

For collecting the amputation data, the amputation wound is illuminated by the broad band light. The reflected light passes through both the LCTFs, which discriminates the light into small band pass wavelengths and are collected by the FPAs. There is an analog to digital converter (ADC) in both the FPAs which digitize the collected images. This digitized data is transferred to the laptops, and used for analysis. The built-in interface in V++ enables the user to set experimental parameters like spectral range, exposure time, binning, tune wait time, and gain. The system, upon initialization tunes the LCTF to the first wavelength and triggers the CCD. The CCD is then exposed for the set exposure time; the ADC digitizes the image and transfers to the respective laptops.

Digital pictures of the wound are also taken using a 6.0 megapixels Canon[TM] PowerShot S3 IS camera, in the same angle as seen by the near-infrared and visible cameras, for aligning the images later.

A 4 x 4 bin is used for acquiring data for both the visible and near-infrared cases. The approximate time for collecting an image cube using the visible and near-infrared cameras is 10 and 30 seconds respectively.

3.7 Data analysis

3.7.1 Determination of the penetration depth

    3.7.1.1 Contrast-to-background ratio

The penetration depth of visible and near-infrared light in the intralipid phantom model was determined by different methods of data analyses. An efficient method is to estimate the contrast-to-background ratio (CBR) of the image cubes collected at different depths of the ink capillary in the suspension. A CBR value is computed for each wavelength in a data cube, and finally, a plot of wavelength vs. depth is made for both the near-infrared and visible data.

Contrast can be defined as the signal emerging out of the ink (in terms of apparent absorbance), which, is the key factor in determining the depth of penetration. Noise (from background), in this case is the signal from regions other than that of the ink capillary, i.e., the intralipid suspension.

A program is written in Matlab, which computes the CBR of the images acquired. Contrast is computed as the difference between the maximum value and minimum value of the apparent absorbance signal from the ink. A particular region of the background is selected from both the sides of the capillary as shown in figure 24 (near-infrared image) and these values are concatenated. The mean value of this concatenated matrix is considered as the noise. Finally CBR is computed as,

$$CBR = contrast / noise$$

Equation 1. Calculation of contrast-to-background ratio

where, contrast = max – min value of the signal region from the ink, and

noise = mean value of the concatenated background matrix.
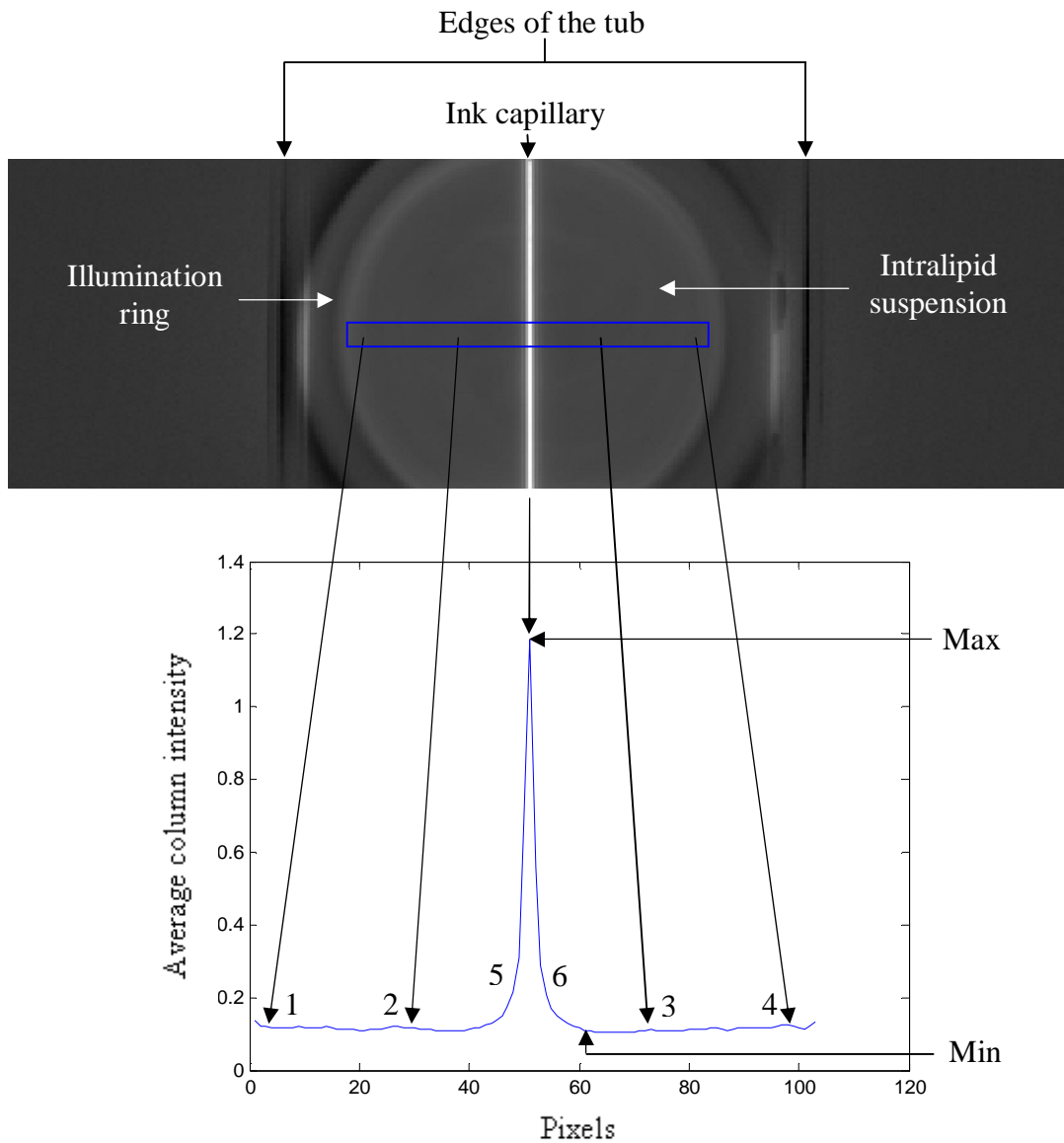
Figure 24. Selection of contrast and noise regions from the image profile

The depth up to which data cubes have to be acquired is given as a user input to the program. The analysis starts with the reference depth, at which the capillary is at the surface of the intralipid suspension, half immersed diameter-wise. The program pulls up the first wavelength image from the filtered set of data for this depth, and prompts the user to crop the image, by clicking on two points in the image, one at the upper left and the other at the bottom right. The user has to make sure that the cropped region (shown in

blue in figure 24) is from the center of the image, which includes the middle part of the capillary and the surrounding suspension. This is done so as to restrict the noise region to the intralipid suspension alone. The coordinates of this region is stored in C drive under the name "points", and is loaded each time a new depth is selected. This is to make sure that the region considered for computing the CBR is the same for all depths (it is important to delete this file or store it in some other location before switching from near-infrared to visible or vice-versa, since the image sizes are different for both the cases). The program then calculates the mean value of each column of pixels in the cropped region (highlighted in blue in the image) and plots a profile out of it. The selection for the regions of contrast and noise, as shown in figure 24 has to be made on this mean column profile. For the noise region, the mouse has to be clicked on the points marked 1, 2 and 3, 4, read into the program as 1 to 2 and 3 to 4, which is concatenated. The concatenated noise region for computing the mean then becomes 1 to 4. The contrast region (shown in between points 5 and 6) is selected by clicking on the max value first and then the min value. The program computes the difference between them and takes it as the value of contrast. The CBR value is computed using equation 1 for all wavelengths (67 in case of near-infrared and 112 in case of visible, due to filtration explained later) at that particular depth. The program then prompts to select the max and min values of the contrast region for the second depth, keeping the noise region the same as in the reference (first) depth. It calculates the CBR value for every wavelength at this depth and this process is repeated for every depth, till the last depth given as the input is reached. The value of CBR is thus computed for all wavelengths at each depth, and stored in a 67 x 15 (wavelength x depth) array called "c2b" in the workspace. The value of 15 for depth

41

indicates that in this analysis, the maximum depth considered for analysis is 15 mm from the reference position. The entire process explained above has to be done separately for computing the CBR for both near-infrared and visible cases. For reliably distinguishing an object, a CBR of at least 2 is required [40]. The threshold for CBR is therefore set at 2. Another method of setting the threshold at 2 is by visually inspecting the images at different depths.

3.7.1.2 Signal-to-noise ratio

Another measure of the penetration depth is realized plainly by replacing the mean taken for the noise region, with the standard deviation. The metric now would be called the signal-to-noise ratio.

$$SNR = signal / noise$$

Equation 2. Calculation of signal-to-noise ratio

The calculation of signal in this case is done in the same way as that in CBR. For computing the noise, the standard deviation, instead of the mean in case of CBR, is taken. Computation of SNR is also done simultaneously by the program explained above, and stored in a separate array of dimension 67 x 15 called "snr", in the workspace.

According to Rose criterion, if the SNR value falls below 5, the image features cannot be distinguished with 100% certainty [43, 44]. This sets 5 as the threshold value for SNR in this experiment.

Another factor that can be determined from the plots for CBR and SNR (shown in the results section) is the wavelength dependency of light penetration. In other words, these methods can be thought of as very useful in determining the wavelengths at which we get the maximum signal out of the capillary, and those at which we get less. This is

since we get a CBR and an SNR value for every wavelength we consider in the visible and near-infrared regions, across all depths. The wavelength band at which we get the maximum values of these parameters for each depth can be considered to be the ones from which useful signal can be efficiently extracted.

3.7.1.3 Michelson Contrast

Percent Contrast is another metric used for the determination of the penetration depth. It quantifies the contrast between the ink capillary and the background. The formula used for this is called Michelson Contrast, defined as

$$(I_{max} - I_{min}) / (I_{max} + I_{min})$$

Equation 3. Calculation of Michelson Contrast

where I_{max} and I_{min} represents the highest and lowest luminances [46].

3.7.1.4 Principal components analysis

Principal components analysis (PCA) is performed on the images collected in the near-infrared and visible ranges to examine whether it would enable seeing deeper than the other methods. PCA is basically a vector space transform used to reduce multidimensional data sets to lower dimensions for analysis. It involves the calculation of the eigenvalue decomposition of a data covariance matrix or singular value decomposition of a data matrix, usually after mean centering the data for each attribute [41].

The major problem faced in this analysis is the selection of the best component image out of all the ones generated by the PCA program, written in Matlab. It is generally noticed that the first few PCA component images give the best contrast between the signal and noise regions, as opposed to the other ones. Therefore the program is made to

43

generate the first 2 component images for every depth and compute their percent contrast using equation 3. This metric is used to determine how deep PCA can help resolve image details and also whether it can do it at a greater depth than the spectroscopic analysis.

3.7.1.5 Multivariate analysis

The amputation wounds are monitored during their healing process and the percent saturation of HbO_2 in the tissue is determined. A routine program written in Matlab was used for processing the data cube obtained. It helps determine the value of the percent saturation of oxyhemoglobin in a selected region of interest.

Determination of this value is basically a twofold process. The measured reflectance spectra are quantified in terms of apparent absorbance, $\mathbf{A}_{xy}(\lambda_i)$, a ratio between the reflected sample radiation, $\mathbf{R}_{xy}(\lambda_i)$, and the reflected radiation from a spectralon which is certified to have ~99.9% reflectance (considered to be a standard), $\mathbf{R}_{xy}(\lambda_i)_0$, measured at wavelengths λ_i for the spatial coordinates x and y [11].

$$\mathbf{A}_{xy}(\lambda) = \log_{10}(R_{xy}(\lambda)_{standard} / R_{xy}(\lambda)_{sample})$$

Equation 4. Calculation of apparent absorbance [11]

The apparent absorbance spectra is deconvoluted into its intrinsic components, oxyhemoglobin and deoxyhemoglobin, and expressed as a percentage of oxyhemoglobin. Prior to deconvolution, the data is filtered using a Savitzky-Golay polynomial filter and also normalized. This, to a good extent reduces the noise in the spectroscopic data. A least-squares fit is performed to deconvolute the measured spectrum for each detector pixel, to determine the best linear combination of oxy and deoxyhemoglobin reference

spectra. The multivariate regression of the spectrum at pixel position (*x, y*) is given below.

$$C_{kj} = S_{k\lambda 1}R_{j\lambda 1} + e_{kj}$$

Equation 5. Multivariate regression matrix

Here, C is a linear, multidimensional, deconvoluted contribution matrix composed of k number of pure components, oxy and deoxyhemoglobin in this case, and j measured samples corresponding to each detector pixel (*x, y*) [11]. The unknown sample data, R, are functions of wavelength, λ_i, and position, j and e_{kj} is a residual matrix associated with regression. The reference spectra generally used for the deconvolution of HbO_2 are of fully oxygenated hemoglobin (100% HbO_2) and completely deoxygenated hemoglobin (100% deoxy Hb). The method of deconvolution was calibrated by assuming a linear relationship between the known value (100% HbO_2 for pure oxyhemoglobin and 0% HbO_2 for pure deoxyhemoglobin) for the given constituent versus its deconvoluted value [11].

The Savitzky-Golay filter used for filtering the spectroscopic data is a moving window low pass filter, which is very helpful in such applications. A Savitzky-Golay filter operates in the time domain, instead of Fourier domain and smoothens the data [42]. Equation 6 given below describes the Savitzky-Golay filter.

$$g_i = \sum_{n = -n_i}^{n_r} c_n f_i + n$$

Equation 6. Savitzky-Golay filter equation [42]

where, $C_n = \{ (A^T \cdot A)^{-1} \cdot (A^T \cdot f_n) \}$,

$A_{ij} = i^j$, $j = 0, 1, 2…..M$. M is the polynomial order,

n_i is the number of data points used on the left of point n and

n_r is the number of data points used on the right of point n.

If in Savitzky-Golay filter, g_i is replaced by a constant (whose estimate is the average), it uses a higher order polynomial, typically quadratic or quartic, i. e., for each point f_i, least square fitting is done for all $n_i + n_r + 1$ points in the moving window, and then g_i is set to be the value of that polynomial at position i. In equation 6, c_n represents the filter coefficients that are derived using the matrices and i is the pixel location. The size of the window used is 15 in this case. Since the filter removes the tail at both the ends of the wavelength ranges, the spectral range is reduced from 650 – 1050 nm to 685 – 1015 nm in the near-infrared range and from 520 – 645 nm to 527 – 638 nm in the visible range.

After filtration, the measured spectrum is deconvoluted for the percent value of oxyhemoglobin, using multivariate least square regression analysis to determine the best linear combination of oxyhemoglobin and deoxyhemoglobin reference spectra.

CHAPTER 4

RESULTS

4.1 Imaging the intralipid phantom model

4.1.1 Estimation of contrast-to-background ratio and signal-to-noise ratio

The intralipid phantom that mimics the properties of tissue is imaged using the multimodal hyperspectral imager and image data cubes are collected at various depths, as mentioned in the methods section. The contrast-to-background ratio (CBR) is calculated for each wavelength, over all depths of the ink capillary tube from the surface of the intralipid suspension. Figure 25 shows the plot for CBR over wavelengths and depths, for the near-infrared data. Corresponding plots for the visible data are shown in figure 26.
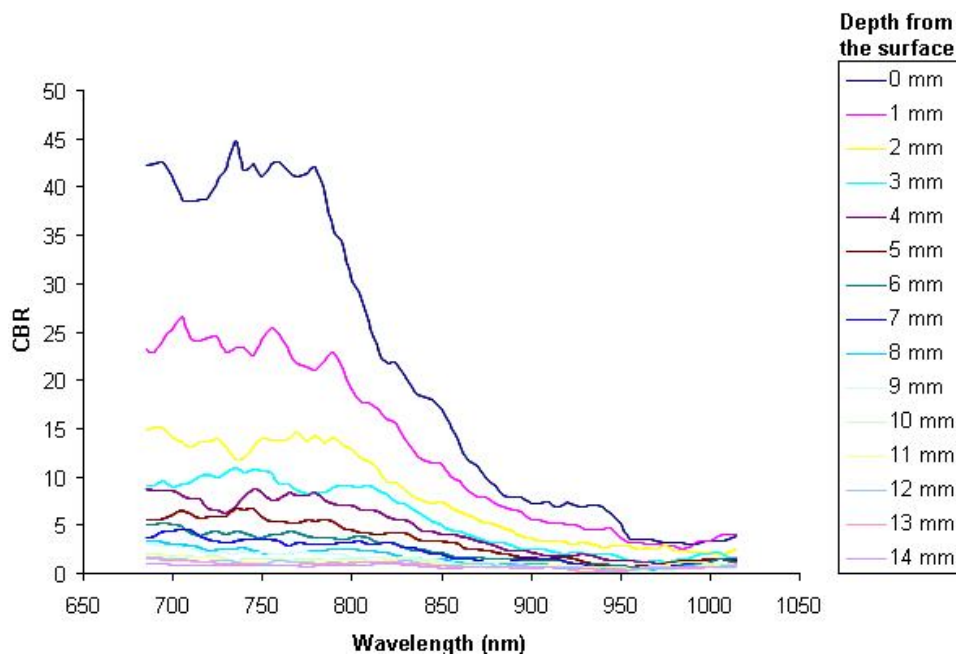

Figure 25. Plot for contrast-to-background ratio of filtered and ratioed near-infrared images
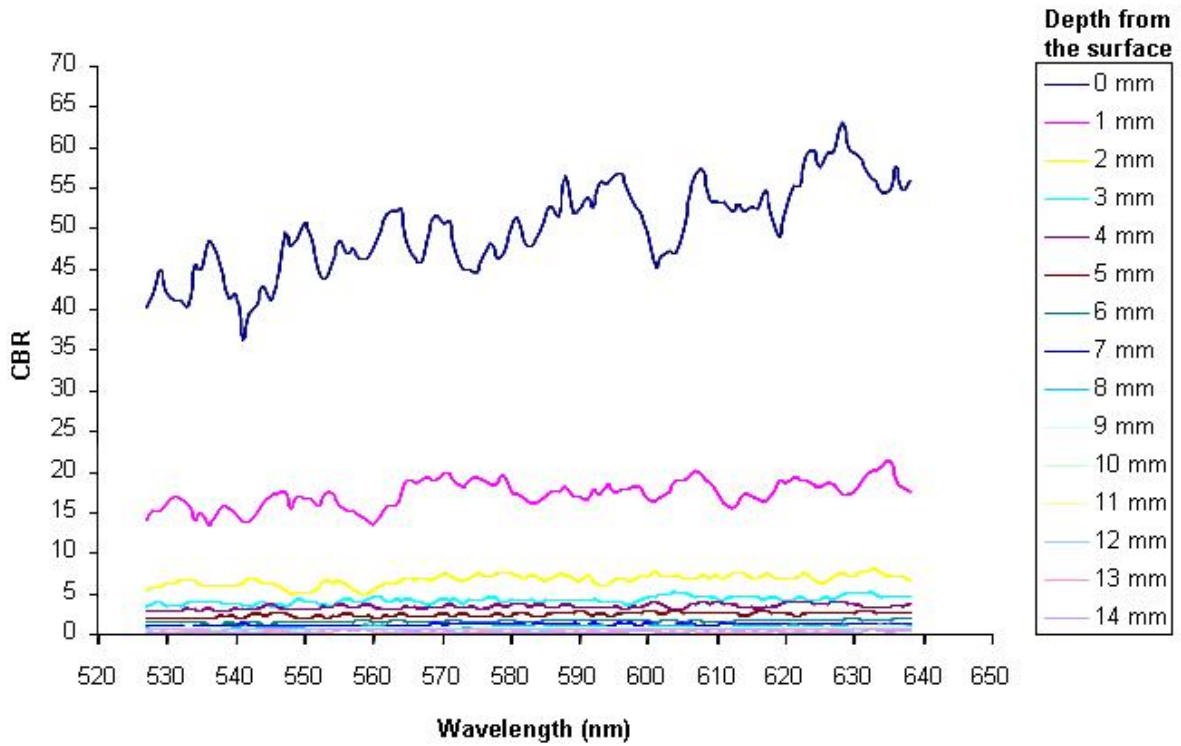
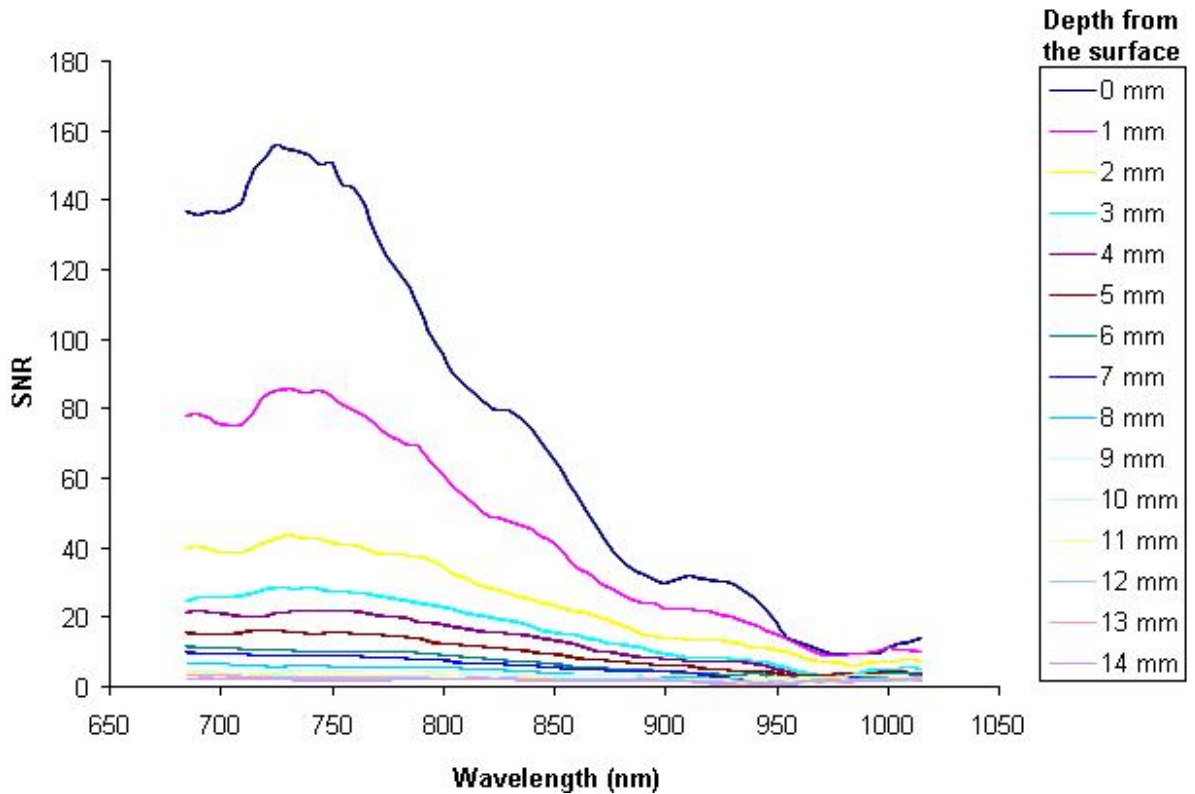**Figure 26.** Plot for contrast-to-background ratio of filtered and ratioed visible images

Figure 27. Plot for signal-to-noise ratio of filtered and ratioed near-infrared images
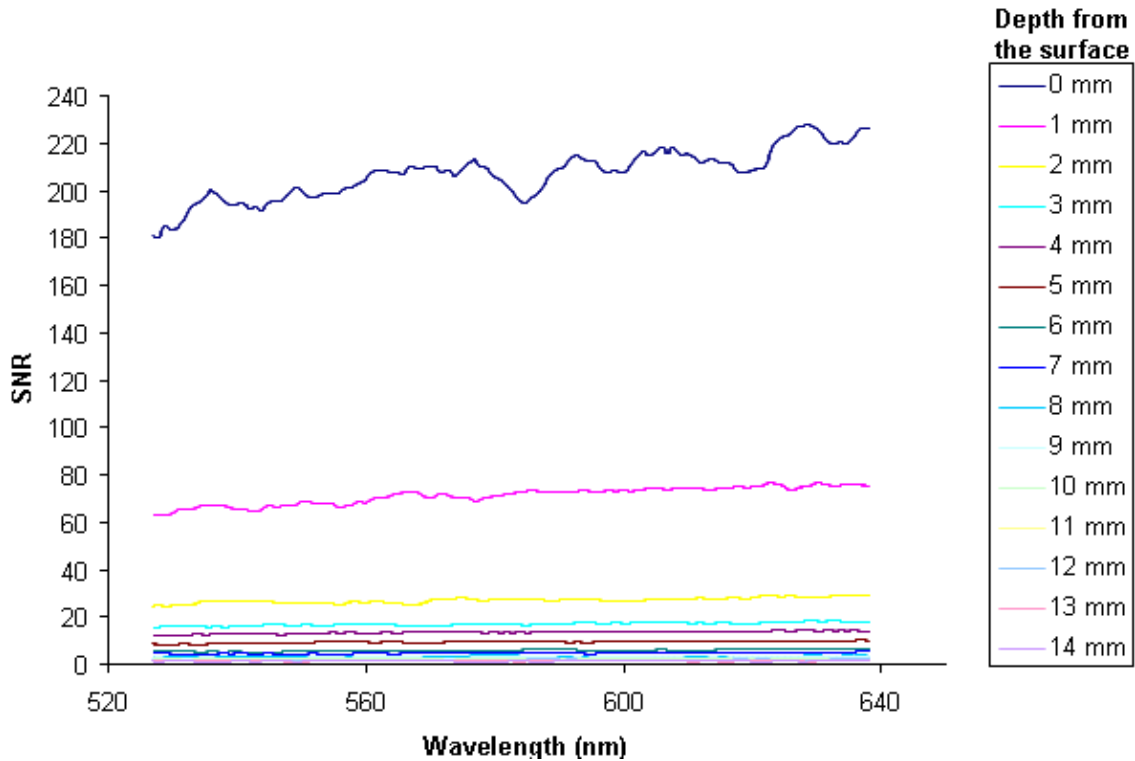
Figure 28. Plot for signal-to-noise ratio of filtered and ratioed visible images

Figures 27 and 28 show the plots for the signal-to-noise ratio for the same data in the near-infrared and visible regions respectively. As explained in the previous section, the signal-to-noise ratio is calculated by replacing the mean (denominator) of the background in CBR with its standard deviation.

The threshold value set for the contrast-to-background ratio is 2. If the value of CBR falls below 2, the object is considered no longer to be reliably distinguishable. Similarly, the threshold set for signal-to-noise ratio is 5, to be certain that image details are identified with 100% certainty [43]. The value of 2 and 5 set as thresholds for CBR and SNR respectively, holds good if the images are visually inspected as well. i.e., the capillary with ink can be clearly distinguished from the intralipid suspension at 9 mm and 6 mm depths respectively in cases of near-infrared and visible images, if visually inspected.

From the plots in figures 25 to 28, it can be clearly seen that there is a dependency of the values of SNR and CBR on the near-infrared wavelengths, whereas it is almost negligible in case of visible data. This dependency owes mainly to the absorption of light by water, which is the major constituent of the intralipid suspension, at higher wavelengths. Due to this, the contrast between the signal and noise regions degrades. This phenomenon is illustrated in the images shown in figure 29, acquired using the near-infrared camera.
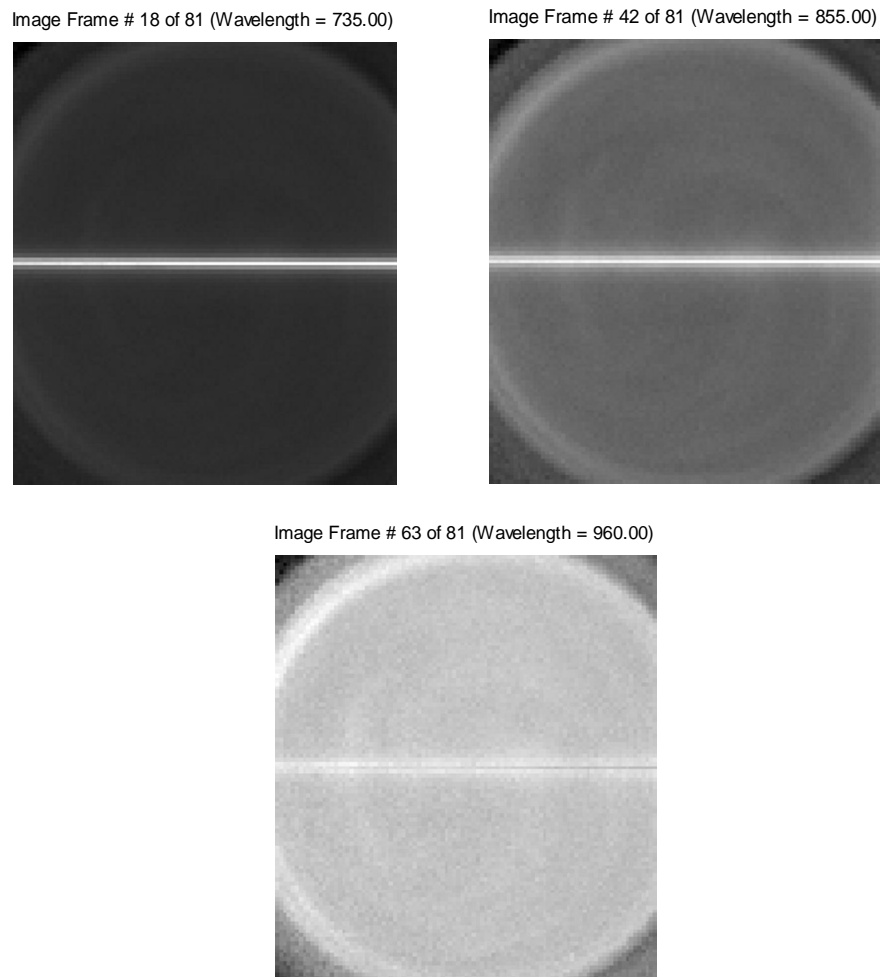

Image Frame # 18 of 81 (Wavelength = 735.00)

Image Frame # 42 of 81 (Wavelength = 855.00)

Image Frame # 63 of 81 (Wavelength = 960.00)

Figure 29. Filtered and ratioed near-infrared images at different wavelengths

The reduction in CBR at higher wavelengths, as mentioned before, can be attributed to the absorption of light by the water in the suspension. At these wavelengths, the signal emerging out of the capillary almost equals the noise due to the behavior of water as an absorber, implying that the CBR value falls at these wavelengths, compared to the smaller ones.

From the above figures and discussion, it can be seen that the value of contrast-to-background ratio falls below 2 when the ink capillary is 9 mm and 5 mm below the surface of the intralipid suspension, for the near-infrared and visible cases respectively. Similarly, keeping a threshold of 5 for SNR, we compute the penetration depth to be 9 mm and 6 mm for near-infrared and visible ranges respectively. Both these cases imply that the near-infrared camera sees deeper into the suspension and therefore in real tissue, than visible. In other words, the image detail resolving power is higher for the near-infrared camera than the visible. Also, there is a higher wavelength dependency in the case of near-infrared, for reasons aforementioned. This finding is the key to the comparison between the phantom model and human tissue, as related to amputation wounds. The threshold regions in the CBR and SNR plots shown in figures 25 to 28 are expanded and shown in figures 30 to 33 for clarity. The thick red plot depicts the depth at which the values fall below the threshold.
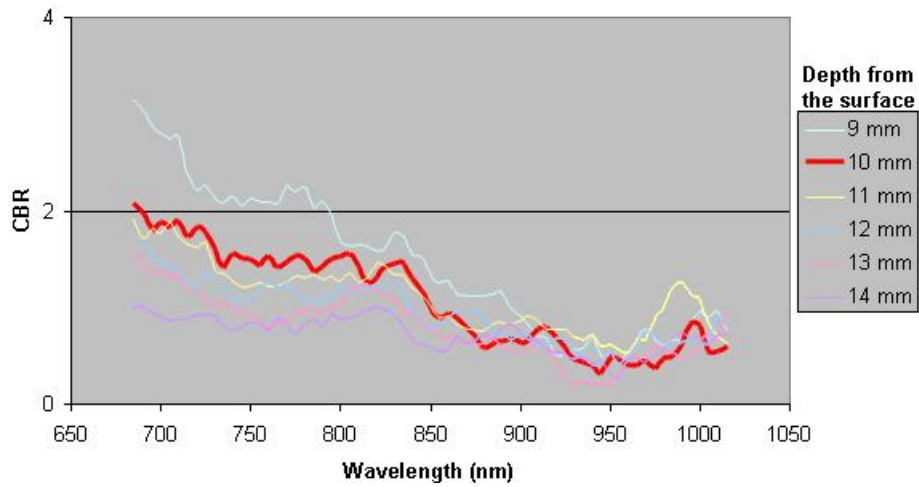
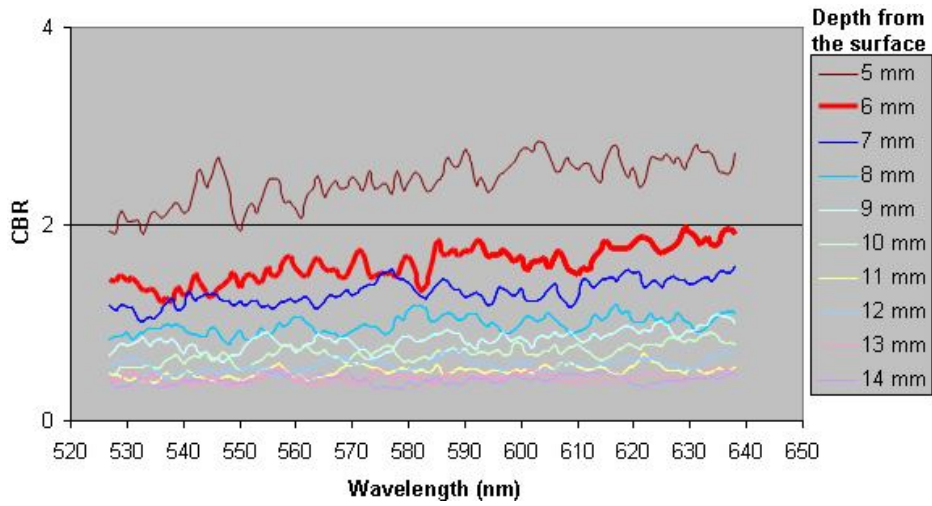**Figure 30.** Expanded CBR threshold region for near-infrared data

Figure 31. Expanded CBR threshold region for visible data
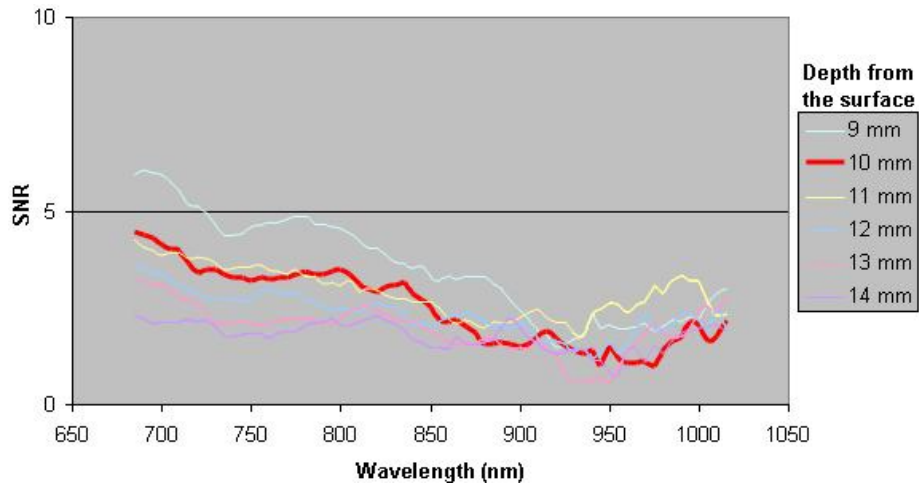

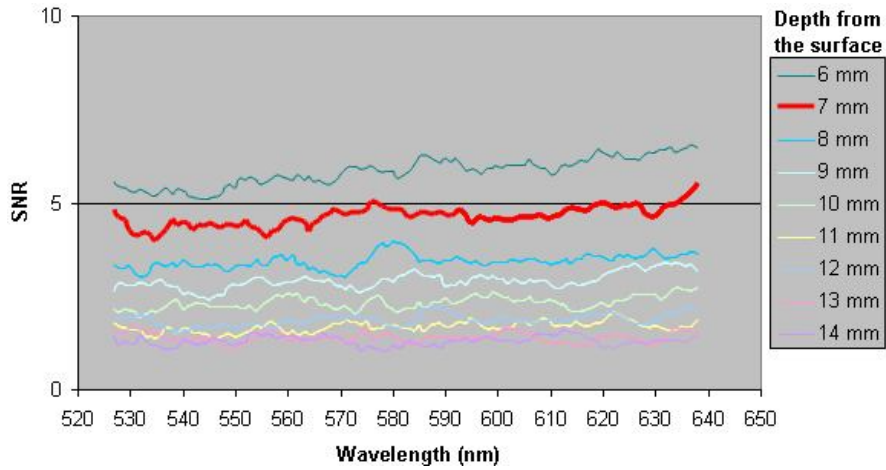**Figure 32.** Expanded SNR threshold region for near-infrared data

Figure 33. Expanded SNR threshold region for visible data

4.1.2 Percent Contrast

The formula given in equation 3 is used to calculate the percent contrast for the near-infrared and visible images. The computation of percent contrast is done only for one image (wavelength) at the region where the CBR and SNR values are high, for every depth. The plots for percent contrast of both the near-infrared and visible images respectively are shown in figures 34 and 35.
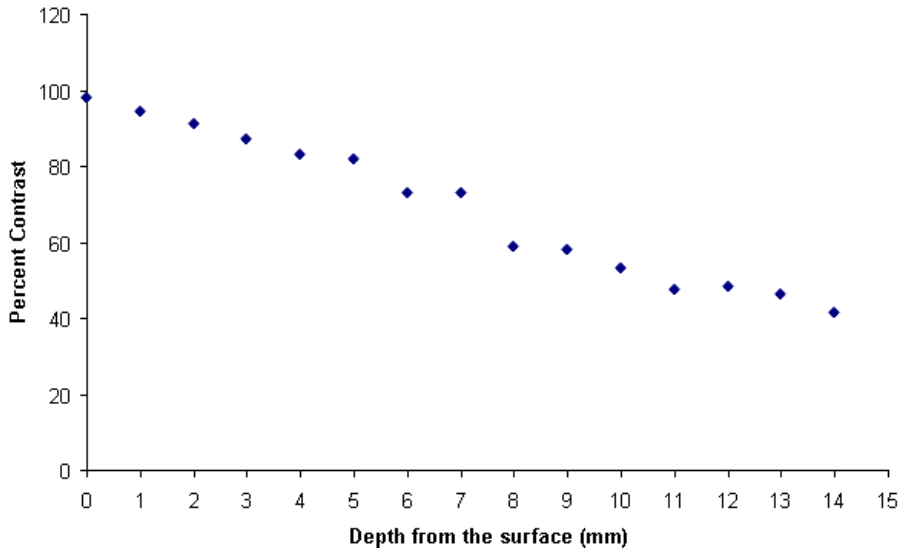

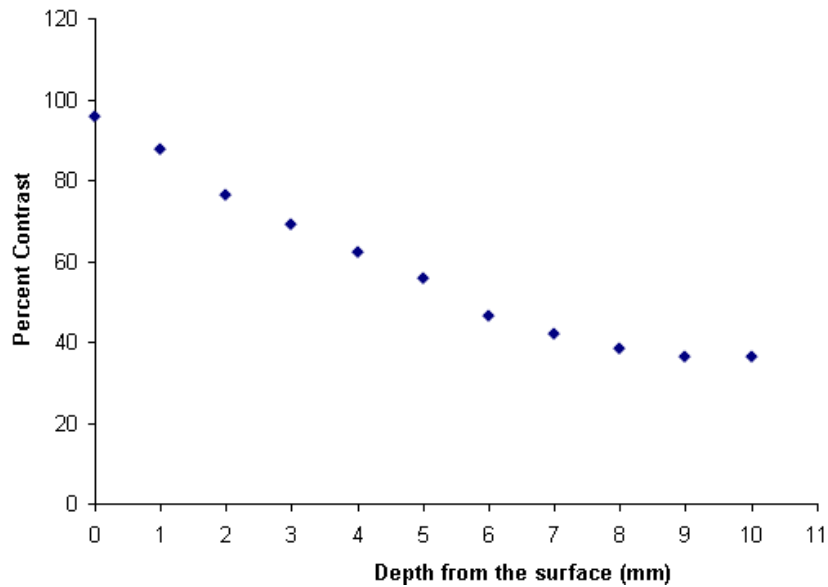**Figure 34.** Plot for percent contrast of near-infrared images

Figure 35. Plot for percent contrast of visible images

According to Rayleigh criterion, neighboring image features are considered to be resolved if the minimum gradient of the signal intensity in the interval between them is equal to ¼ of maximum intensity, i.e., threshold contrast 25% [47]. But since the profile for plotting the percent contrast becomes noisy at depths 14 mm and 10 mm respectively for near-infrared and visible images, we stop here and consider these values as the depths at which the image features can be clearly resolved. Using percent contrast as a metric also demonstrates that the near-infrared light penetrates deeper than visible, into the phantom model.

4.1.3 Principal Components Analysis (PCA)

PCA is performed on the near-infrared and visible data to examine whether it enables seeing deeper than the types of analyses described in the previous sections. The first three PCA image components in the near-infrared data when the ink capillary is at the surface of the suspension is shown in figure 36 as an example to demonstrate the higher contrast of those images.
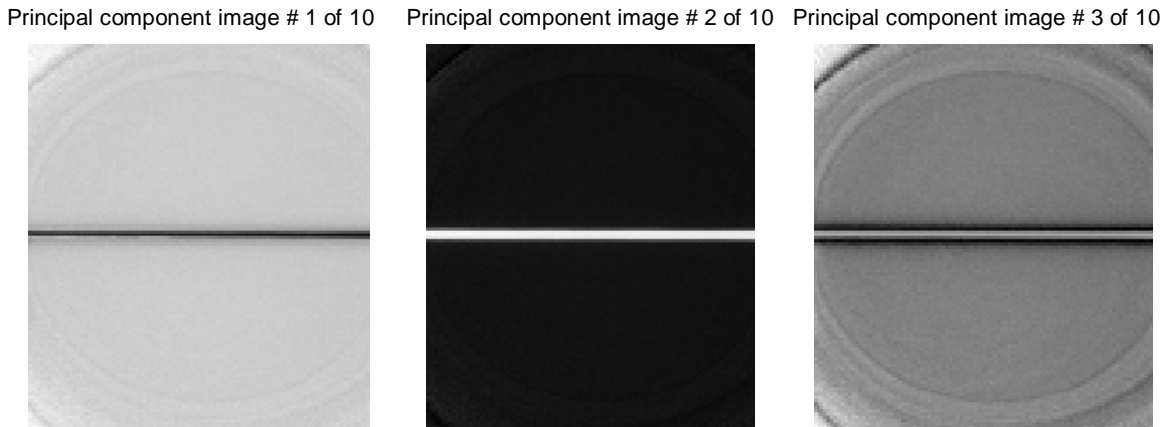
Figure 36. The component images generated for the near-infrared data when the capillary is at the surface

From the figure it can be clearly noticed that the first two component images are superior in terms of contrast. A comparison between all the first PCA component images for near-infrared data for depths of the capillary from 9 mm to 16 mm in the suspension is also shown in figure 37. Similarly, near-infrared images for depths from 9 to 11 mm are shown in figure 38, for a comparison.

The only metric used for determining the resolving ability of PCA is percent contrast, since the mean of the background for computing the CBR varies widely within the images at different depths, and may sometimes reach infinitely high values, contributing to widely varying values of CBR. This is due to the inherent noise in PCA component images, as can be seen from those in figure 37.

It can also be seen from these images that the capillary tube with ink is visible in the images, even up to 16 mm. Therefore it can be concluded from the images in figures 37 and 38, and the plots in figures 39 and 40 that PCA helps see deeper in terms of contrast with the background, though the penetration depth is difficult to be estimated as

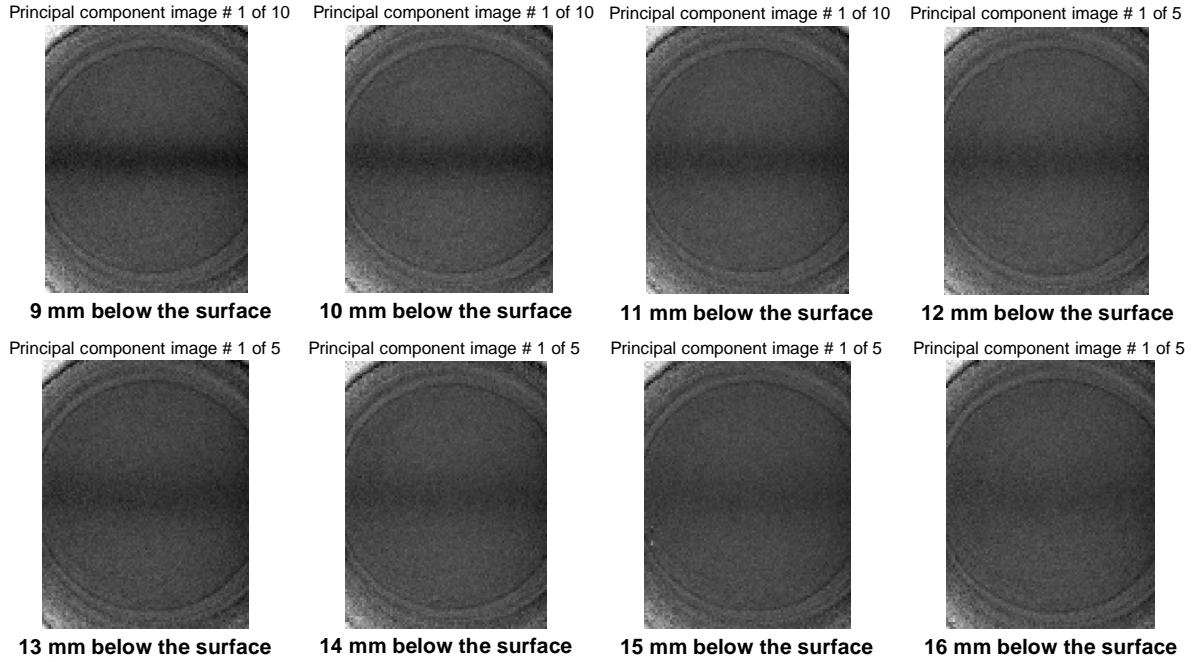in case of other types of analyses, due of the dependability of the metric on the best component image.

Principal component image # 1 of 10 | Principal component image # 1 of 10 | Principal component image # 1 of 10 | Principal component image # 1 of 5

9 mm below the surface **10 mm below the surface** **11 mm below the surface** **12 mm below the surface**

Principal component image # 1 of 5 | Principal component image # 1 of 5 | Principal component image # 1 of 5 | Principal component image # 1 of 5

13 mm below the surface **14 mm below the surface** **15 mm below the surface** **16 mm below the surface**

Figure 37. First PCA component images for depths from 9 mm to 16 mm for the near-infrared data

Image Frame # 19 of 81 (Wavelength = 740.00) Image Frame # 19 of 81 (Wavelength = 740.00) Image Frame # 19 of 81 (Wavelength = 740.00)

9 mm from the surface **10 mm from the surface** **11 mm from the surface**
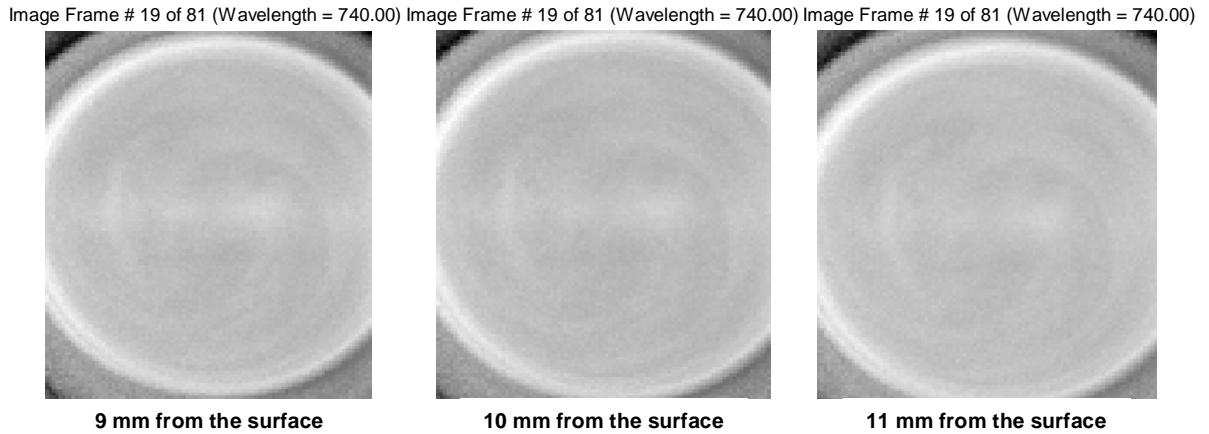
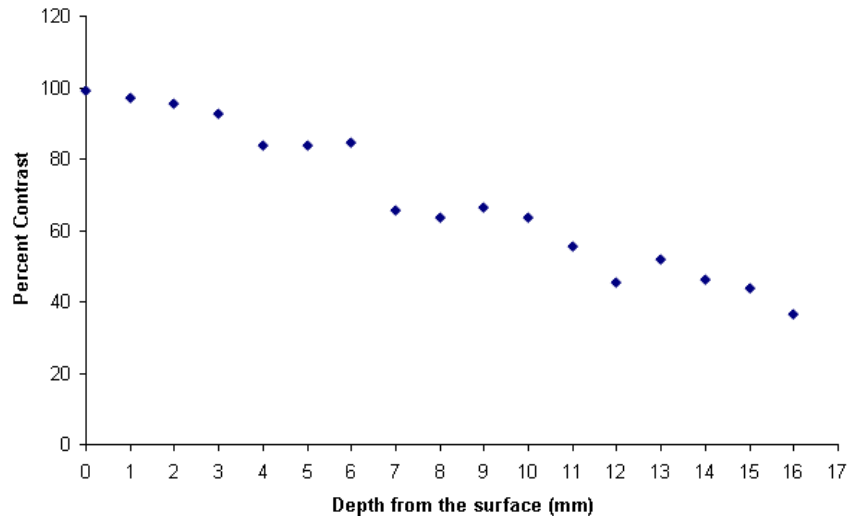**Figure 38.** Near-infrared images for depths from 9 mm to 11 mm

Figure 39. Percent contrast for near-infrared PCA component image #2 over various depths
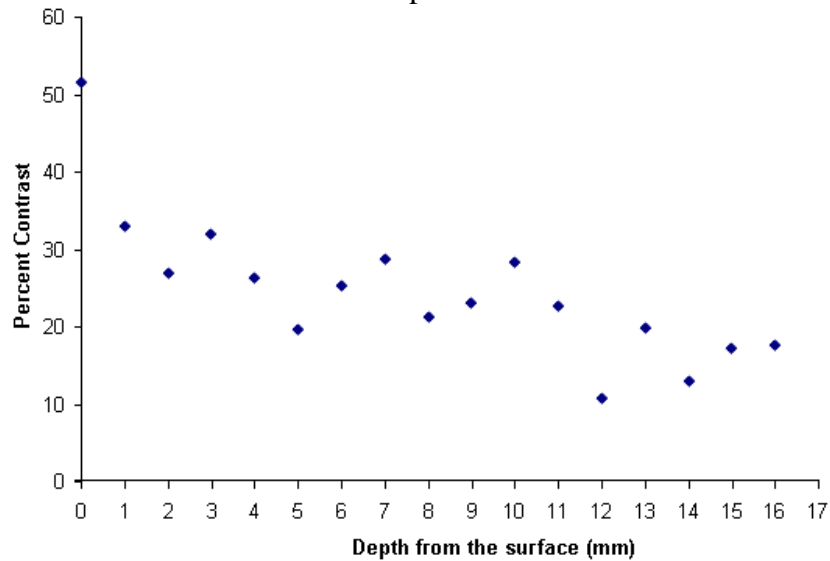

Figure 40. Percent contrast for visible PCA component image #2

The values of the percent contrast curve are not as smooth as those in the spectroscopic analysis, owing to the inherent noise that the PCA images tend to have. Though this is the case, it can be seen that PCA helps resolve image details at a greater depth than the other method, by means of the images and plots.

Figures 41 to 44 compare near-infrared and visible PCA images when the ink capillary is approximately 3 and 7 mm under real animal (beef) fat layers.

Principal component image # 1 of 10   Principal component image # 2 of 10   Principal component image # 4 of 10
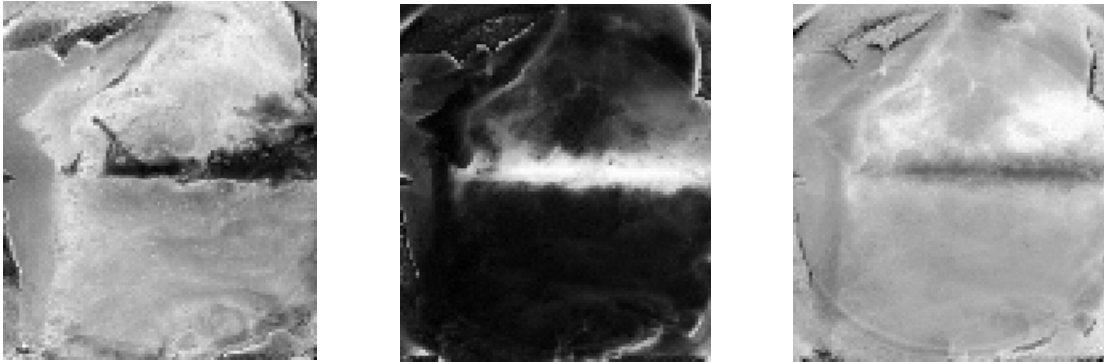
Figure 41. Near-infrared PCA component images for the ink capillary ~3 mm below the surface of the fat layer

Principal component image # 1 of 10   Principal component image # 2 of 10   Principal component image # 3 of 10
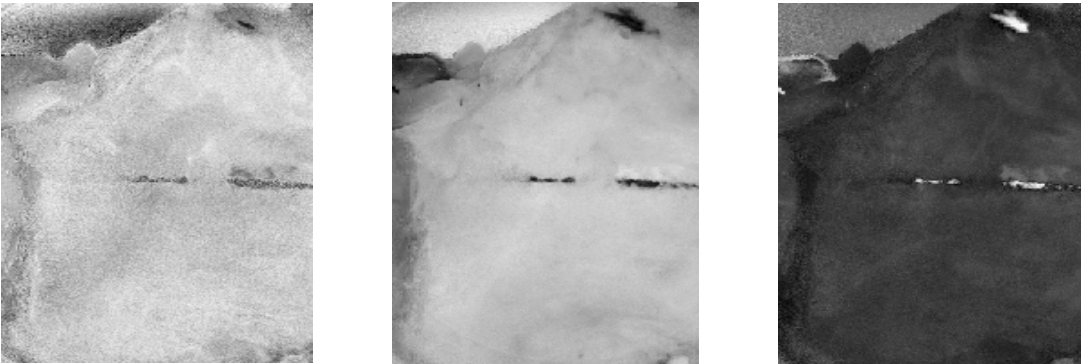
Figure 42. Visible PCA component images for the ink capillary ~3 mm below the surface of the fat layer

Principal component image # 2 of 10   Principal component image # 5 of 10   Principal component image # 6 of 10
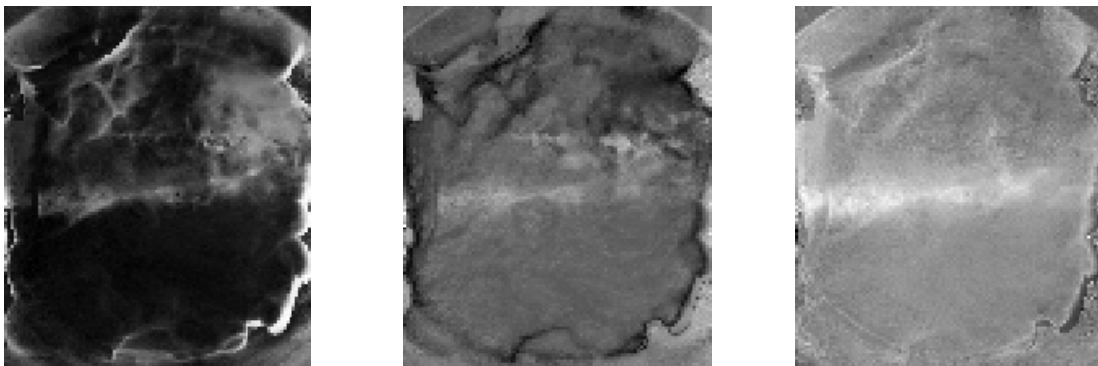
Figure 43. Near-infrared PCA component images for the ink capillary ~7 mm below the surface of the fat layer

Principal component image # 1 of 10   Principal component image # 3 of 10   Principal component image # 4 of 10
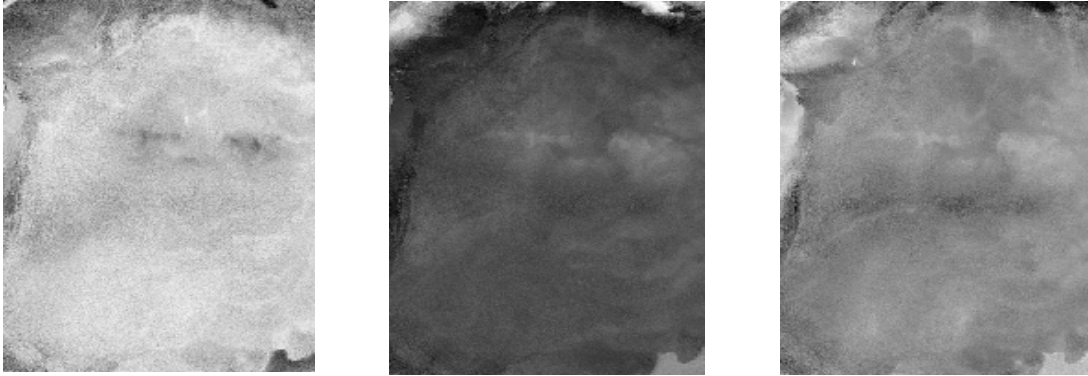

Figure 44. Visible PCA component images for the ink capillary ~7 mm below the surface of the fat layer

It can clearly be seen that the near-infrared PCA component, in both the cases (~3 and 7 mm), can resolve the ink capillary prominently than the visible ones. This is again a proof for the higher resolving ability of near-infrared images, compared to visible.

4.2 Penetration depth

From the value of CBR, the depth up to which the near-infrared camera can detect the signal from the capillary is 9 mm from the surface of the suspension, and for visible, it is 5 mm. Corresponding values when using SNR as the metric are 9 mm and 6 mm for the near-infrared and visible cases respectively.

Using PCA analysis gives a good contrast for images still deeper. i.e., the images details can be resolved with greater ease at depths which cannot be reached by the spectroscopic analysis method. Using PCA as a metric also results in demonstrating the higher ability of the near-infrared camera than the visible, in resolving image details, as can be seen from the images of the phantom model and real beef fat.

4.3 Comparison of the results with the amputation data

The information about depth of penetration of near-infrared and visible light in the intralipid model obtained through different methods of analyses will be used in this section to monitor the blood perfusion in amputation wounds.

It is evident that the near-infrared light penetrates deeper into the tissues, than visible light. In other words, the near-infrared camera has a better ability than the visible to resolve image details at different depths. Applying this theory to the amputation data acquired, and by examining the images and plots in figures 45 and 46, the following conclusion can be arrived at: the oxyhemoglobin saturation in the deeper tissues shoots high after the amputation, and then gradually decreases and reaches a homeostatic state. In the case of superficial tissue, it is initially low and gradually rises to a higher value.

The data for the plots in figure 46 is that of a left above knee amputation (AKA) done on a patient who was monitored four times, over a period of nine days. From the plots for percent saturation of oxyhemoglobin for both the near-infrared and visible cases, it can be seen that the percent HbO_2 at both the selected regions (A and B) on each image, though initially high, reduces by a small amount over the monitored period, in the near-infrared case. It happens in the reverse order in the case of visible data. The percent oxyhemoglobin value shoots up over the period of monitoring, in the case of visible data. This fact is further supported by the near-infrared and visible images shown in figure 49, which depicts the level of oxyhemoglobin in an amputated region on another subject, monitored twice, post-amputation. The trend explained holds true even in this case. Figures 47, 48, and 50, 51 demonstrate this trend respectively for the near-infrared and visible cases, for the two amputation cases considered. The multivariate analysis

performed on near-infrared data necessarily provides a good estimate of the percent saturation of oxyhemoglobin in the deeper tissue, and visible data, that in the superficial tissue layer (by virtue of the near-infrared camera seeing deeper than the visible). It is therefore proved that the multimodal hyperspectral imaging can be used for non-invasively monitoring the *in vivo* saturation of oxyhemoglobin in both the deeper and superficial tissues of amputation wounds.
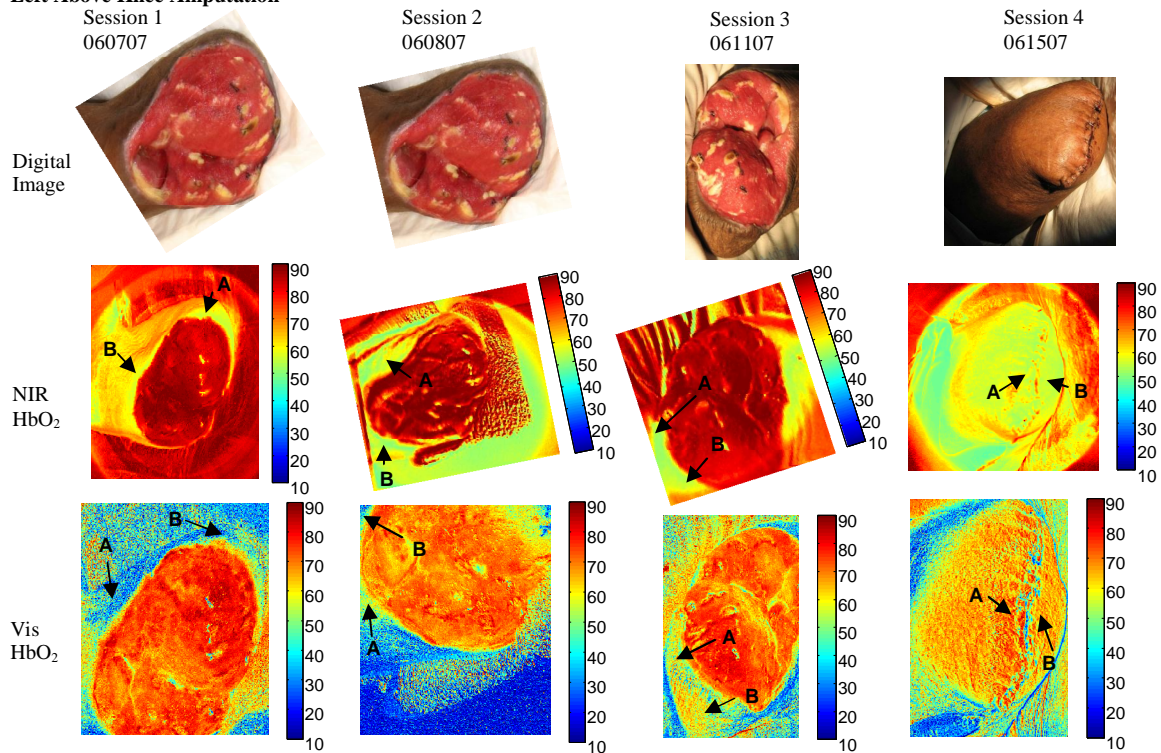

Figure 45. Digital images of the amputated region with corresponding near-infrared and visible images, generated using multivariate analysis technique
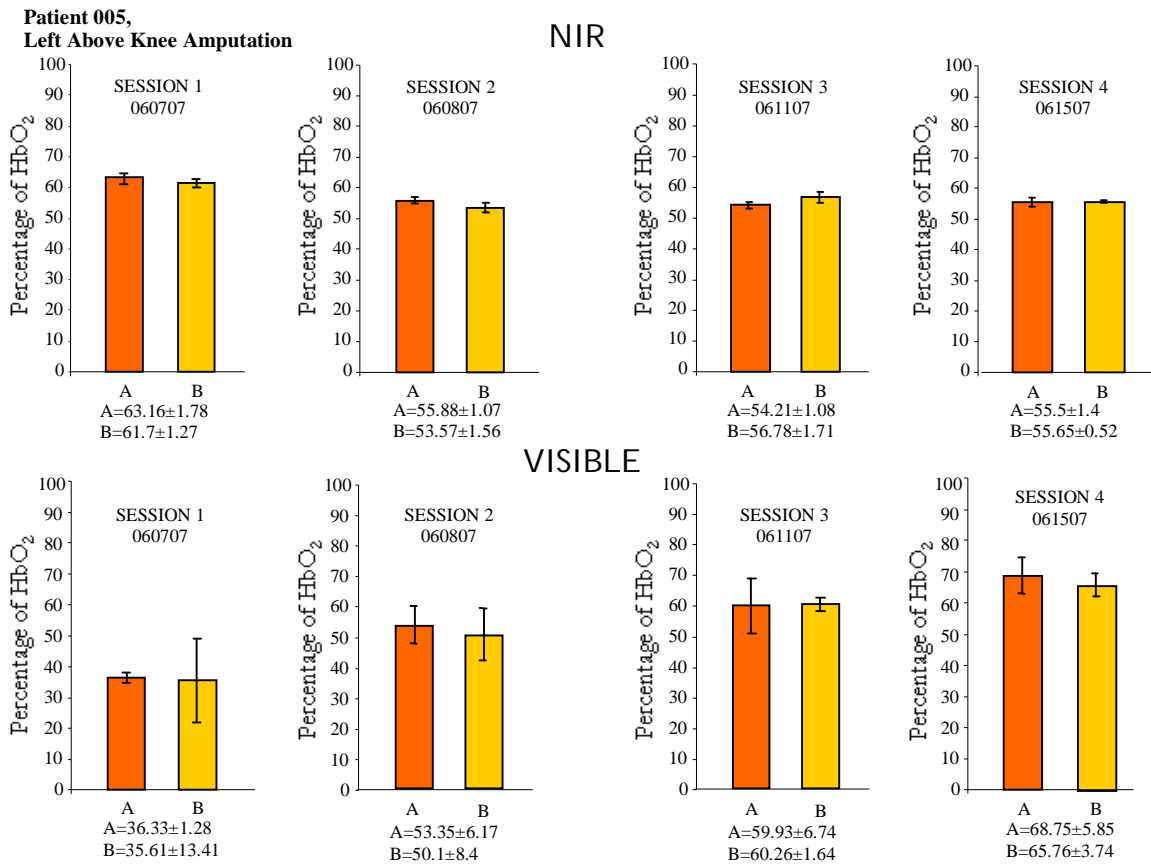
Figure 46. Bar graphs showing the percent saturation of oxyhemoglobin and standard deviation over four sessions for the corresponding near-infrared and visible images

Figure 47. Near-infrared data showing the variation in the percent saturation of oxyhemoglobin at the two selected points for the first amputation case

Figure 48. Visible data showing the trend in the variation of percent HbO$_2$

**Patient 002,
Monitoring Post Amputation
Left Lower Limb**

Session 1
051707

Session 2
052107

NIR
HbO$_2$

A1=76.5±6.5
B1=84.5±2.1

A2=68.9±1.7
B2=67.6±1.1

Vis
HbO$_2$

A1=62±3.9
B1=62±1.2

A2=70±4.2
B2=70±3.2

Figure 49. Digital images of the amputated region with corresponding near-infrared and visible images, generated using multivariate analysis technique
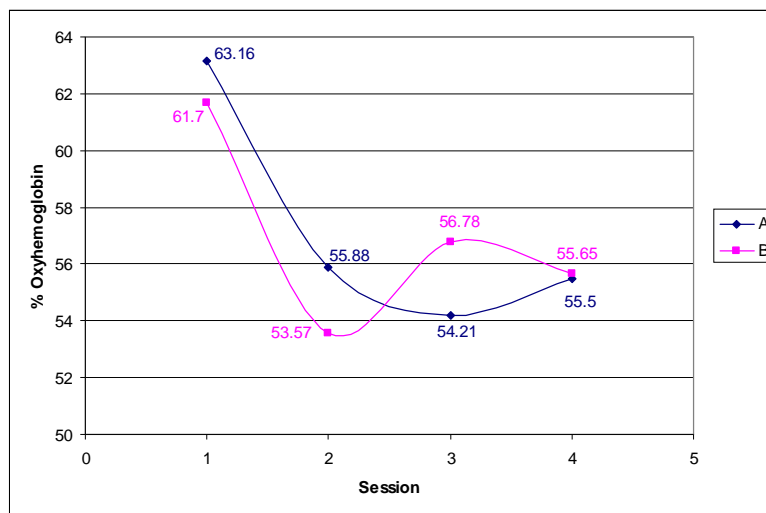
63

Figure 50. Near-infrared data showing the variation in the percent saturation of oxyhemoglobin at the two selected points for the second amputation case
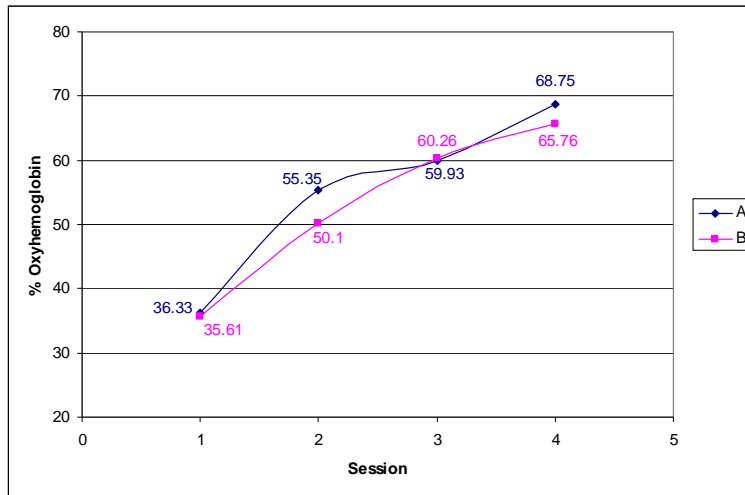

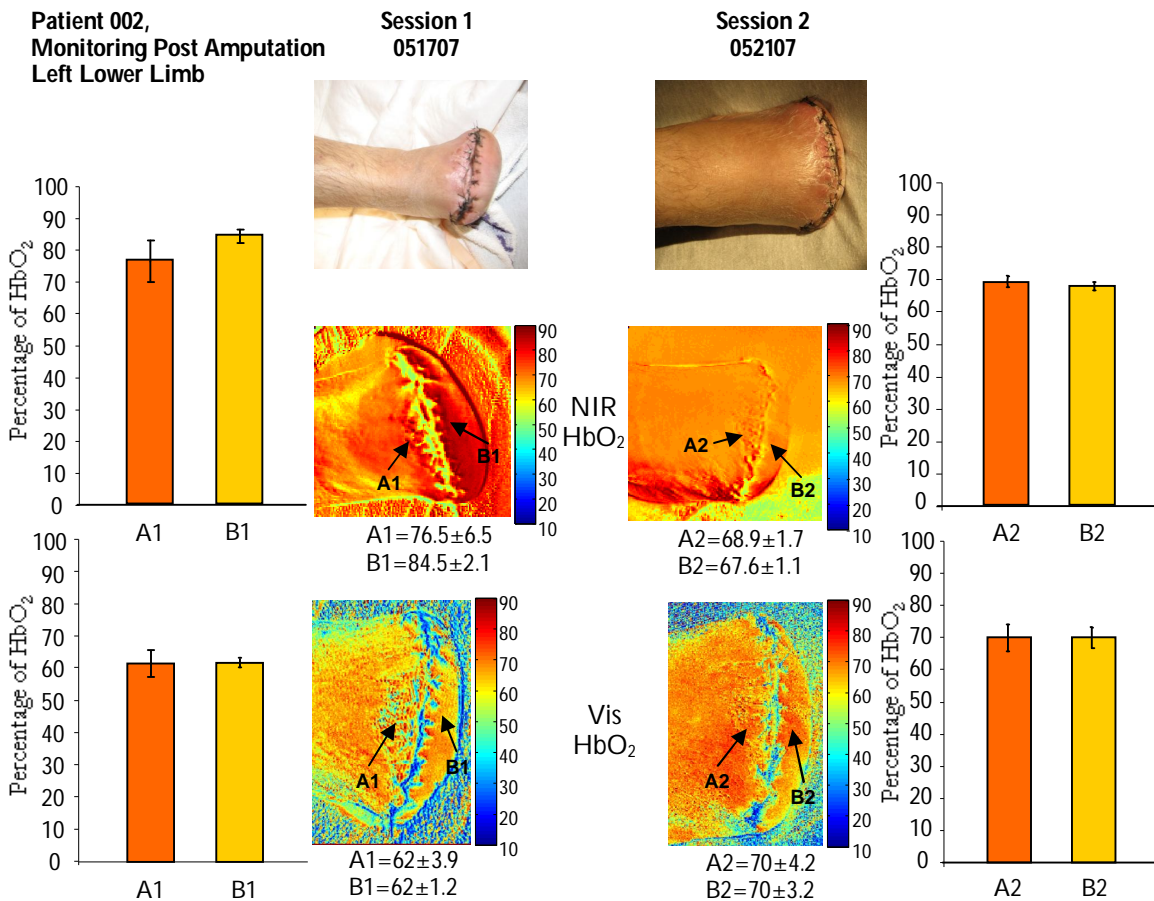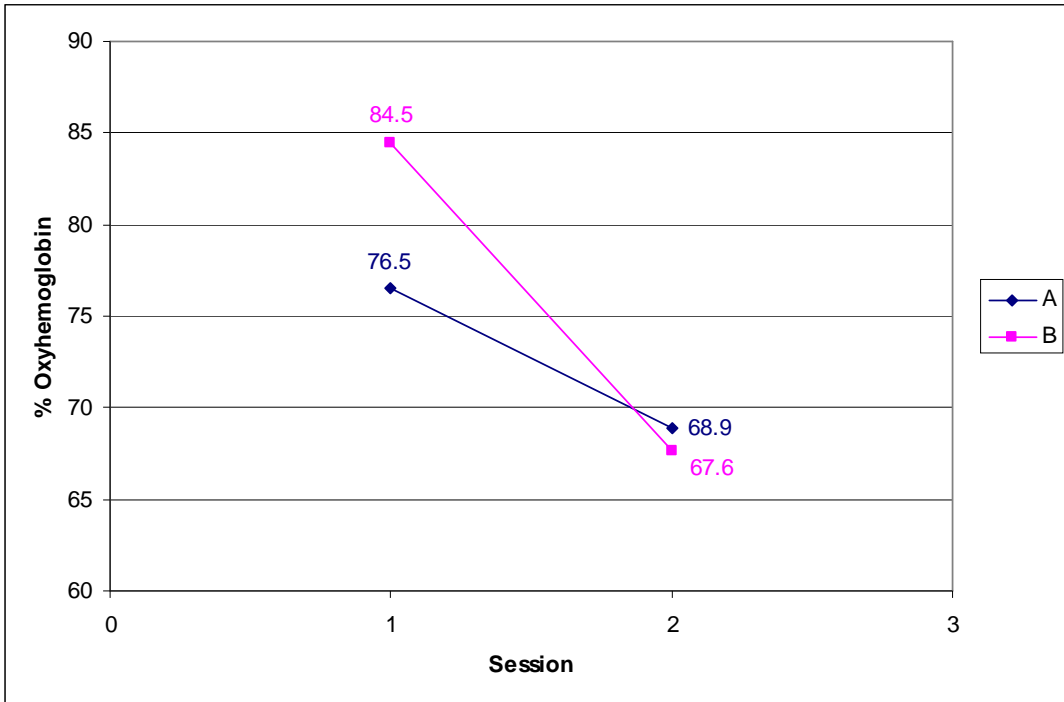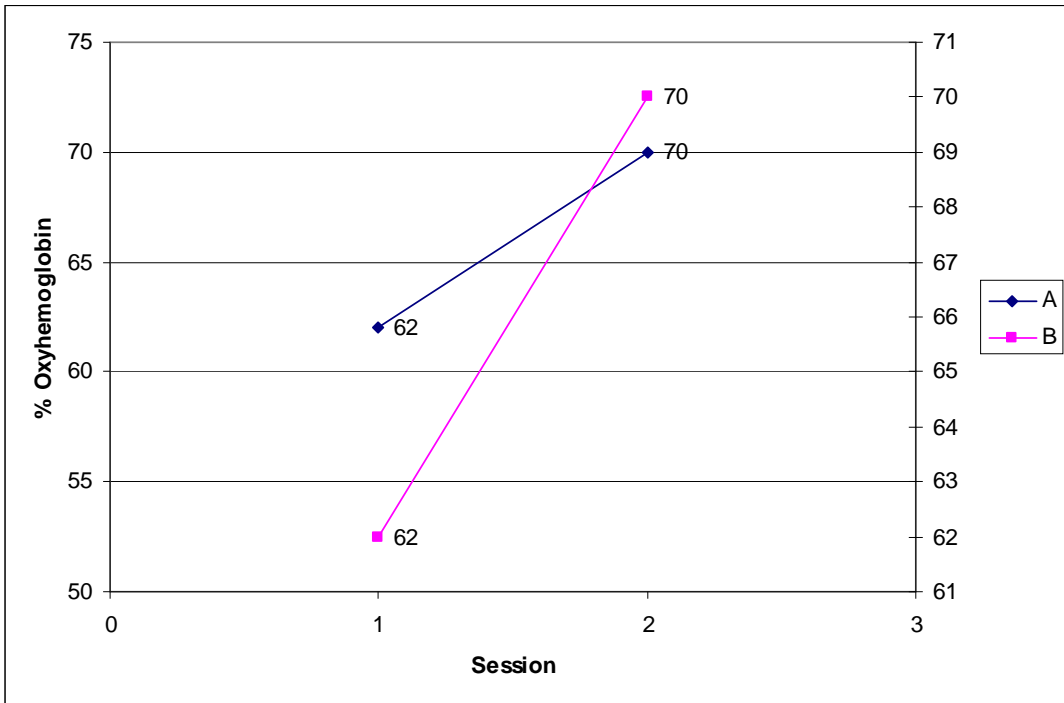**Figure 51.** Visible data showing the trend in the variation of percent HbO_2
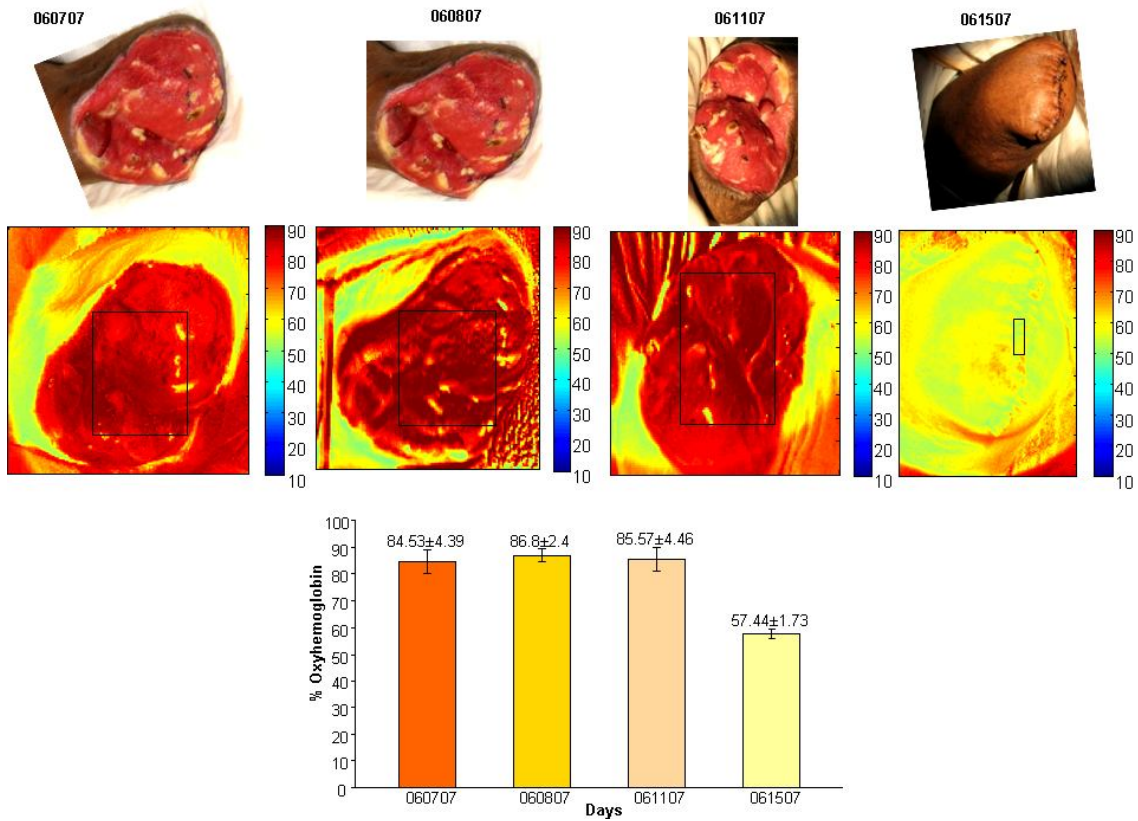
Figure 52. Near-infrared images and percent HbO$_2$ plots for different sampling areas of case 1
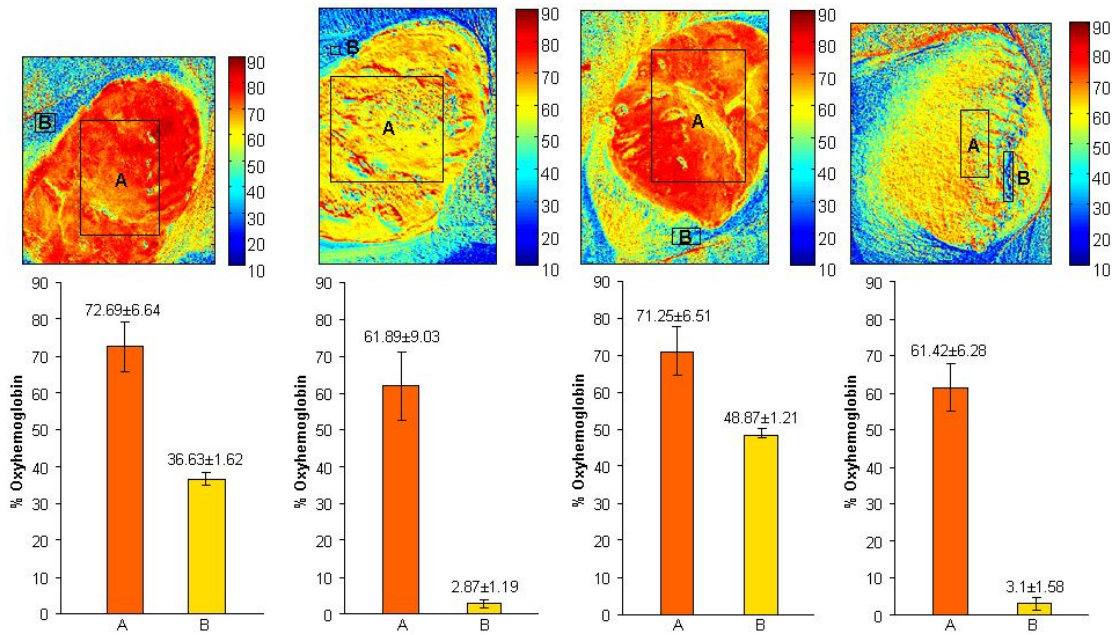
Figure 53. Visible images and percent HbO$_2$ plots for different sampling areas of case 1

The figures 52 and 53 show different sampling regions for the amputation in case 1. It gives an estimate of the percent saturation of oxyhemoglobin at the meaty region and also on the suture.

Speaking about the application of this technique for monitoring amputation wounds, surgeons can utilize it to efficiently determine the amount of perfusion of oxygenated blood in both the deeper and superficial tissues, which would serve as a good estimate of the process of healing. If there is not enough perfusion of blood at some amputated area of the limb, the surgeons would still have the option of locating a portion above the current one, where there is good (or better) blood perfusion and performing a second amputation.

CHAPTER 5

DISCUSSION

There is wide variety of applications for the hyperspectral imaging technique in the field of agriculture, physics and military and also in the remote sensing of satellites. Its application in the medical field though, is relatively new. The peculiarity of hyperspectral imaging lies in the fact that it renders spectral information in each pixel, across an integrated set of wavelengths. It has broad range of applications in medicine, like the one discussed here.

The monitoring of a surgical wound in terms of the percent saturation of oxyhemoglobin is very important since it enables the surgeon to ascertain that the patient is recovering normally from surgical trauma. This research was focused on the determination of the image detail resolving abilities of near-infrared and visible camera systems and translation of those results to utilize the multimodal hyperspectral imager for monitoring an amputation wound. This technique aids the surgeon in non-invasively determining (quantifying) the perfusion of blood in the deeper and superficial tissues, *in vivo*, in terms of percent saturation of oxyhemoglobin.

Several methods of image/data analyses were done on image data cubes of an intralipid phantom model which mimics the optical properties of a skin-tissue interface collected using multimodal hyperspectral imaging technique. The research established

that near-infrared light penetrates deeper into tissues than visible light. All the types of analyses done on the images gave concrete evidence for the above mentioned fact.

This rendered the determination of oxyhemoglobin saturation in amputation wounds easy. The near-infrared amputation data showed a high percent saturation of oxyhemoglobin in the tissues, which gradually decreased by a small level. The visible data, though initially had a low level of percent HbO_2, demonstrated a steady increase in this level, over a period of time. This phenomenon, by virtue of the fact that the near-infrared camera sees deeper into tissues than the visible camera, explains the perfusion of blood in both the deeper and superficial tissues.

CHAPTER 6

CONCLUSIONS AND FUTURE GOALS

The ability to resolve image details by utilizing a hyperspectral imager, at different depths and wavelengths spanning the visible to near-infrared in an intralipid suspension modeling human tissue were determined and it was noticed to be higher in the near-infrared system. Different signal processing techniques and chemometrics were used in the analysis of data cubes collected by both the camera systems.

The multimodal hyperspectral imaging system developed at the Laboratory of Biomedical Imaging, UTA enables surgeons to non-invasively analyze the *in vivo* percent saturation of oxyhemoglobin in tissues. It helps them monitor amputation wounds over a period of time. For justifying the validity of this technique, a proof of principle study was done on an intralipid phantom model, and the results were used in real amputation data obtained from the clinic, to determine the perfusion of blood in both the deeper and superficial tissue layers.

This system can be further enhanced to deliver better results and greater speed and ease of operation. An improvisation to the existing system can be done by incorporating a light source controlled using a Digital Light Processing chip (DLP®) (from Texas Instruments), with the FPA, instead of the LCTF. This would improve the spectral range greatly.

A camera which has higher sensitivity would also help improve the image detail, and can reduce the acquisition time. A major problem while acquiring hyperspectral images is the motion artifacts exhibited in the region of imaging due to movement of body parts, especially while imaging surgical and clinical data. Image registration algorithms, which can take care of this problem, if developed would help minimize errors and artifacts.

REFERENCES

1. http://en.wikipedia.org/wiki/Amputation

2. http://en.wikipedia.org/wiki/Gangrene

3. http://www.podiatrytoday.com/article/7396

4. Khaodhiar L, Dinh T, Schomacker KT, et al. The use of medical hyperspectral technology to evaluate microcirculatory changes in diabetic foot ulcers and to predict clinical outcomes. Diabetes Care, Apr 2007; 30(4):903-910.

5. Jing B, Tianxin G, Kui Y and Nanguang C. Locating inhomogeneities in tissue by using the most probable diffuse path of light. Journal of Biomedical Optics, March/April 2005; 10(2):024024(1-9).

6. Kye Jin J, In Duk H, Sangjoon H and Gilwon Y. Comparison between transmittance and reflectance measurements in glucose determination using near infrared spectroscopy. Journal of Biomedical Optics, January / February 2006; 11(1):014022(1-7).

7. Manuela L, Ambrogio C, Bruno F, Stefano T and Renato M. A phantom with tissue-like optical properties in the visible and near infrared for use in photomedicine. Lasers in Surgery and Medicine, July 2001; 28:237-243.

8. Driver I, Feather JW, King PR and Dawson JB. The optical properties of aqueous suspensions of Intralipid, a fat emulsion. Phys. Med. Biol., June 1989; 34(12):1927-1930.

9. Kothare A. Visible reflectance hyperspectral imaging system with improved capabilities for translational medicine projects. University of Texas at Arlington, 2005.

10. Gat N. Imaging spectroscopy using tunable filters: A Review. SPIE, 2000; 4056: 50 – 64.

11. Zuzak KJ, Schaeberle MD, Lewis NE and Levin IW. Visible reflectance hyperspectral imaging: Characterization of a noninvasive, in-vivo system for determining tissue perfusion. Anal. Chem., May 2002; 74(9):2021-2028.

12. Zuzak KJ, Schaeberle MD, Gladwin MT, Cannon RO III, and Lewin IW. Noninvasive determination of spatially resolved and time-resolved tissue perfusion in humans during nitric oxide inhibition and inhalation by use of a visible reflectance Hyperspectral imaging technique. Circulation, 2001; 104 (24):2905 – 2910.

13. http://www.medterms.com

14. http://www.cri-inc.com/assets/components/VariSpec/VariSpec_Brochure.pdf

15. http://www.cri-inc.com/files/VariSpec_Brochure.pdf

16. http://www.cri-inc.com/products/components.asp

17. Morris HR, Hyot CC and Treado PJ. Imaging Spectrometers for Fluorescence and Raman Microscopy: Acousto-Optic and Liquid Crystal Tunable Filters. Applied Optics, 1994; 48: 857 – 866.

18. Poger S and Angelopoulou E. Selecting components for building multispectral sensors. IEEE CVPR technical sketches (CVPR Tech Sketches). IEEE Press, New York. 2001.

19. Slwason RW, Ninkov Z and Horch E. Hyperspectral Imaging: Wide-Area Spectrophotometry Using a Liquid-Crystal Tunable Filter. Publication of the Astronomical Society of the Pacific, 1999; 111:621 – 626.

20. Miller PJ. Use of Tunable Liquid Crystal Filters to Link Radiometric and Photometric Standards. Metrologia, 1991; 28:145 – 149.

21. VariSpec ^{TM} Liquid Crystal Tunable Filter User's Manual, Cambridge Research and Instrumentation.

22. http://www.nikonusa.com/template.php?cat=1&grp=5&productNr=1902

23. PIXIS system user manual, Princeton Instruments.

24. http://content.piacton.com/Uploads/Princeton/Documents/Datasheets/PIXIS%20400%20Rev%20B0.pdf

25. Etaloning in Back Illuminated CCD's. Roper Scientific Inc., (http://content.piacton.com/Uploads/Princeton/Documents/Whitepapers/etaloning.pdf)

26. http://www.photomet.com/coolsnap.html

27. The Basics of Camera Technology, Technical Manual, SONY.

28. CoolSNAP Interline Camera, Roper Scientific Inc., (Source: http://www.piacton.com/pdfs/whitepapers/interline.pdf)

29. Shah B. Characterization of a Non-Invasive, in-vivo Microscopic Hyperspectral Imaging System for Microvascular Visualization. University of Texas at Arlington, 2006.

30. Leal MJ. Effect of Pixel Size and Scintillator on Image Quality of a CCD-Based Digital X-ray Imaging System. Worcester Polytechnic Institute, 2001.

31. http://www.photomet.com/software/software_pvcam.php

32. Getting Started with V++, User manual, Digital Optics Ltd.

33. 'The Newport Resource' 2008-2009. Newport Corporation pp 111.

34. 'The Newport Resource' 2008-2009. Newport Corporation pp 132.

35. 'The Newport Resource' 2008-2009. Newport Corporation pp 137 – 138.

36. 'The Newport Resource' 2008-2009. Newport Corporation pp 140 – 141.

37. http://www.newport.com/file_store/Supporting_Documents/Tech_Ref_Spectral_Irradiance37.pdf

38. http://www.rxlist.com/cgi/generic/intralipid20.htm

39. http://en.wikipedia.org/wiki/Spectralon

40. http://www.phys.cwru.edu/courses/p431/notes-2003/node123.html

41. http://en.wikipedia.org/wiki/Principal_components_analysis

42. Press WH, Flannery BP, Teukoslky SA, Vetterling WT. Numerical Recipes in C: The Art of Scientific Computing, NY: Cambridge University Press, 1992.

43. http://en.wikipedia.org/wiki/Signal-to-noise_ratio

44. Bushberg JT et al. The Essential Physics of Medical Imaging. Philadelphia: Lippincott Williams & Wilkins, 2006; p.280.

45. Taroni P, Pifferi A, Torricelli A, Cubeddu A. Time-resolved Optical Spectroscopy and Imaging of Breast. Opto-Electronics Review, 2004; 12(2):249 – 253.

46. http://en.wikipedia.org/wiki/Contrast_(formula)

47. Boris Polonsky A and Oleg Protopopov D. Spatial Resolution Limitation in Auger Microanalysis of Compounds. Mikrochimica Acta, 1994; 114(1):413 – 419.

BIOGRAPHICAL INFORMATION

Tinsy John Perumanoor was born on 24th June, 1980 in Pathanamthitta, Kerala, India. He completed his Diploma in Medical Electronics in June 2001 from the State Board of Technical Education, Kerala, India and Bachelor of Engineering in Electrical and Electronics Engineering in April 2004 from Bharathiar University, Tamil Nadu, India. He then worked for two years as Research Associate on a project on Magnetic Bearings sponsored by the Ministry of Human Resource Development, Govt. of India, at the National Institute of Technology Calicut, Kerala. After this he joined the Master of Science program in Bioengineering at the University of Texas at Arlington in Fall 2006. His current research area is hyperspectral imaging, applied in the field of medicine. Apart from this he has good interest in electronic equipment design, and other imaging modalities like X-ray and ultrasound.